Nonsmooth simulations of 3D Drucker-Prager granular flows and validation against experimental column collapses

Gauthier Rousseau, Thibaut Métivet, Hugo Rousseau, Gilles Daviet, Florence Bertails-Descoubes

Nonsmooth simulations of 3D Drucker-Prager granular flows and validation against experimental column collapses

Gauthier Rousseau[1,2,4] †, Thibaut Métivet[1] ‡, Hugo Rousseau[3,2], Gilles Daviet[1] ¶, and Florence Bertails-Descoubes[1] ||

[1]Univ. Grenoble Alpes, Inria, CNRS, Grenoble INP, LJK, 38000 Grenoble, France

[2]Environmental Hydraulics Laboratory, École Polytechnique Fédérale de Lausanne, Lausanne, Switzerland

[3]Univ. Grenoble Alpes, INRAE, UR ETNA, 38000 Grenoble, France

[4]Institute of Hydraulic Engineering and Water Resources Management, TU Wien, Karlsplatz 13, 1040, Vienna, Austria

(Received 9 November 2022; revised xx; accepted xx)

In this paper, transient granular flows are examined both numerically and experimentally. Simulations are performed using the 3D nonsmooth numerical granular model introduced in Daviet & Bertails-Descoubes (2016*b*), which represents the granular medium as an inelastic and dilatable continuum subject to the Drucker-Prager yield criterion in the dense regime. One feature of this numerical model is to resolve such a nonsmooth rheology without any regularisation, by leveraging tools from nonsmooth optimisation.

We show that this nonsmooth simulator, which relies on a constant friction coefficient, is able to reproduce with high fidelity various experimental granular collapses over inclined erodible beds, provided the friction coefficient is set to the avalanche angle - and not to the stop angle, as generally done. Our results, obtained for two different granular materials and for bed inclinations ranging from 0° to 20°, suggest that a simple constant friction rheology choice remains reasonable for capturing a large variety of granular collapses up to aspect ratios in the order of 10.

We further investigate the precise role of the frictional walls by performing experimental and simulated collapses with various channel widths. We find out that, unlike some assumptions formerly made in the literature, the channel width has lower influence on the granular flow.

Finally, we extend the constant coefficient model with an hysteretic model, thereby improving the predictions of the early-stage dynamics of the collapse. This illustrates the potential effects of such phenomenology on transient flows, paving the way to more elaborate analysis.

Key words: Granular collapses, continuum material, Drucker-Prager rheology, nonsmooth optimisation, quantitative validation, hysteresis

† gauthier.rousseau@gmail.com
‡ thibaut.metivet@inria.fr
¶ gdaviet@gmail.com
|| florence.descoubes@inria.fr

1. Introduction and related work

Granular materials exhibit state-transitions: under specific pressure and shear rates, the grain assembly may either behave as a fluid, a solid or a gas (Andreotti *et al.* 2013). As an example, avalanches first flow over complex topographies as viscoplastic fluids and ultimately stop their course as a static solid deposit. Similarly, during granular impact cratering, the falling object ejects grains outwards, forming a gaseous entity for a brief instant. Performing efficient and reliable predictions of such flows remains challenging and raises several issues, from the fundamental underlying theory to applied industrial or geophysical processes.

In this context, two families of numerical approaches have been employed: the *Discrete Element Method (DEM)*, which consists in modelling the dynamics of each grain and its interactions, and the *continuum-based* method, which describes the granular material at a macroscopic scale, relying on rheological closures to capture the phase transitions and relate the state of stress to the material deformation. By modelling inter-grain forces such as friction, adhesion or elasticity, DEM is the most *ab initio* approach to simulate the behaviour of granular materials, and has been used extensively to simulate various model experiments in unsteady (Staron & Hinch 2005; Lacaze *et al.* 2008) or steady (Silbert *et al.* 2001; Da Cruz *et al.* 2005; Azéma & Radjai 2014) regimes, yielding valuable insights about the relation between the microstructure and the macroscopic properties. However, DEM inherently suffers from high computational costs, which in practice restricts its use to small-scale systems. In contrast, continuum methods provide opportunities to simulate larger scale scenarios using depth-averaged (Naaim *et al.* 2003; Balmforth & Kerswell 2005; Moretti *et al.* 2012) or full two- or three-dimensional (Lagrée *et al.* 2011; Dunatunga & Kamrin 2015; Gaume *et al.* 2018) fluid models, factoring most of the microstructure complexity in macroscopic constitutive laws.

Many studies in the last decade have therefore focused on the formulation of such rheological closures, using model experiments such as the plane shear or inclined plane set-ups. The main feature of granular materials is the presence of a pressure-dependent yield stress, characterised by an internal friction coefficient μ, which sets the threshold on the maximal sustainable ratio of the shear stress over the pressure before flow, $\tau/p \leqslant \mu$. Experimental methods found in the literature to estimate the internal friction coefficient of a material are diverse, ranging from the use of the avalanche angle or the ang

As such, the $\mu(I)$ rheology is able to capture two crucial features of granular flows: (i) the existence of a minimal shear stress for the material to keep flowing, described by the *stop friction coefficient* $\mu_s = \tan\theta_s$ (with θ_s the corresponding *stop angle*) and (ii) the presence of shear-rate-dependent viscous dissipation at large inertial number $I > I_0 \sim 0.3$, precisely responsible for the existence of steady flows in a range of applied shear rates.

While extensive testing of the $\mu(I)$ rheology has been performed in many steady-flow contexts, highlighting its robustness for the prediction of inertial flows, its prediction of a monotonic increase of the friction coefficient with I is however unable to describe the transition from rest to flow characterised by the existence of a static friction coefficient larger than the dynamic friction coefficient (Hutter & Koch 1991; Pouliquen & Forterre 2002; Da Cruz *et al.* 2002). This friction gap results, for instance, in an hysteresis effect in avalanches: when inclining a container initially filled with static grains, the material starts to flow at a higher *avalanche angle* θ_a (corresponding to a friction $\mu_a = \tan\theta_a$) than the angle of repose.

This suggests that for very small I, the $\mu(I)$ is a decreasing function from $I = 0$ to some

small $I^* > 0$ value. Exploring the $I < 10^{-2}$ behaviour, DeGiuli & Wyart (2017) suggested that $\mu(I)$ is indeed non-monotonic, exhibiting a decrease from $\mu(I = 0)$ to $\mu(I_* \sim 10^{-3}) = \mu_s$ which amplitude $\Delta_{\mu,hyst}$ is induced by endogenous acoustic noise depending on grain rigidity and applied pressures.

Among the different model experiments available to study granular flows at low inertial number I, the simple collapse of a granular column onto a flat or inclined surface is one of the most studied yet distinctive cases. Closely reminiscent of natural avalanches or landslides, it challenges both the accuracy of constitutive laws in *friction-dominated*, *unsteady* and *hysteretical* regimes, and the sensitivity of granular flows to boundary conditions.

Following the encouraging agreement between DEM simulations and the local $\mu(I)$ rheology obtained by Lacaze & Kerswell (2009) for axisymmetric collapses on horizontal planes, the continuum numerical studies of Lagrée *et al.* (2011), Ionescu *et al.* (2015), Martin *et al.* (2017) or Chupin *et al.* (2021) have explored the relevance of this rheology in the context of unsteady flows, and simulated granular flows using a viscoplastic fluid framework. While these studies report good scaling predictions, the quantitative comparisons with experiments from Farin *et al.* (2014) performed by Ionescu *et al.* (2015); Martin *et al.* (2017) seem to require the introduction of higher friction coefficients than the ones measured using the usual steady flow experiment.

As mentioned by Lagrée *et al.* (2011), the use of a constant friction coefficient in their viscoplastic model also seems to reproduce the simulated collapses fairly accurately, but at the expense of adjusting the coefficient. This questions the actual role of the $\mu(I)$ rheology in this context, but also highlights the need for close comparisons between simulations and experiments, in order to assess the domain of validity of rheological laws with a constant friction coefficient and better understand the role and calibration of this coefficient.

Contributions

In this paper, we focus on the relevance of a unique constant friction coefficient to predict accurately granular collapses on inclined planes. To this end, we perform *numerical simulations* at the continuum level, both in 2D and 3D, as well as *experiments* of granular column collapses over erodible beds with slopes varying from 0° to 20°. We model the granular material as a dilatable, fully plastic continuum with a Drucker-Prager yield surface and non-associated flow rule. We solve the resulting nonsmooth rheology without any regularisation by leveraging the Sand6 software (https://gitlab.inria.fr/elan-public-code/sand6), a numerical scheme introduced by Daviet & Bertails-Descoubes (2016*a*,*b*) and inspired from nonsmooth optimisation algorithms originally developed in the context of rigid body contact dynamics (Moreau 1994).

To evaluate the role of the constituting grains, we consider two different granular materials, composed of either 0.5 mm spherical glass beads similar to the ones used by Pouliquen (1999); Jop *et al.* (2006), or coarser irregular granules (using the terminology of Andreotti *et al.* (2013)) found in natural sediments like sand. We characterise the macroscopic parameters of each material using avalanche and inclined chute setups; it is noteworthy that for the glass beads, we retrieve the same stop angle behaviour as Pouliquen (1999) and follow-up works using similar beads.

We perform numerical simulations of the inclined collapses using the $\mu(I)$ rheology or a constant friction coefficient, set either from the experimental *avalanche* or *stop* angles, and compare them with the experiments, faithfully accounting for the boundary conditions and the lifting door. Our results do not only confirm the weak impact of a $\mu(I)$ rheology in this context, but also show that experimental granular collapses with various slopes, flume widths, and aspect ratios, are better predicted by setting a constant friction coefficient equal

to the (higher) *avalanche* angle, as opposed to the usual (lower) stop angle provided by the Pouliquen (1999) or Pouliquen & Forterre (2002) experimental protocols.

Studying the effect of wall friction on collapses in narrow flumes with variable width, we furthermore show that a linear rescaling of the two-dimensional friction coefficient as observed by Savage (1979); Taberlet *et al.* (2003); Jop *et al.* (2005) and used by Ionescu *et al.* (2015) to simulate collapses in two-dimensions is still valid but with a much smaller effective granular flow depth.

Overall, our conclusions significantly deviate from those of previous works, which model granular collapses by using a $\mu(I)$ rheology based on the stop friction coefficient (Lagrée *et al.* 2011; Dunatunga & Kamrin 2015; Ionescu *et al.* 2015). Our results may suggest that unsteady collapses are more likely governed by local transitions from rest to flow. Along the paper, we support our observations by validating carefully our simulator against experiments and/or prior art in a number of well-controlled scenarios.

The paper is organised as follows: we present in section 2 our modelling strategy combining an exact Drucker-Prager yield criterion with usual fluid conservation equations, along with our constraint-based approach to solve for the corresponding non-regularised discrete equations (c.f. section 2.3). We show in section 2.4 that our numerical model is self-consistent using a numerical avalanche test. We then describe our different experimental set-ups for studying granular collapses and measuring macroscopic parameters in section 3, and validate our numerical model with a constant friction coefficient on model experiments in section 4, before showing its predictive potential on collapses of natural sediments. We further analyse experimentally and numerically the impact of the lateral walls – in combination with the initial column aspect ratio – during granular collapses in section 5. Finally, we extend our plain Drucker-Prager rheology with a simple hysteretic law, and illustrate the important role of such description to predict the dynamics of transient collapses in section 6.

The maintained C++ Sand6 software implementing the semi-implicit scheme to solve the continuum conservation equations with the Drucker-Prager rheology, used to study the role of the unique friction coefficient is available at https://gitlab.inria.fr/elan-public-code/sand6. Simulations of the experimental collapses were performed using a fork of the Sand6 code available at https://gitlab.com/groussea/sand6py which provides a python binding of the C++ library along with analysis scripts.

2. A nonsmooth numerical model for Drucker-Prager flows

In this section, we present our continuum dilatable Drucker-Prager plastic fluid model for granular flows, along with the nonsmooth numerical discretisation used to robustly and efficiently simulate true-scale collapses. The numerical model is based on the original reformulation of the Drucker-Prager rheology as a conic constraint introduced in Daviet & Bertails-Descoubes (2016*a*,*b*), and implemented in the open-source Sand6 software.

In order to assess the physical relevance of this model in the context of transient granular flows, we numerically reproduce a classical avalanche experiment in two and three dimensions, and analyse the role of the Drucker-Prager friction coefficient in regards to the usual experimental avalanche and stop friction coefficients.

2.1. *Continuum modelling*

Focusing on the large deformation regimes, we model the granular material as a continuous yield-stress fluid and introduce the corresponding strain-rate tensor

$$\dot{\boldsymbol{\epsilon}} = \frac{1}{2}\left(\nabla \boldsymbol{u} + \nabla \boldsymbol{u}^T\right) \tag{2.1}$$

with $\boldsymbol{u} \equiv \boldsymbol{u}(\boldsymbol{x}, t)$ the velocity of the material in Eulerian coordinates. We also introduce the volume fraction field $\phi(\boldsymbol{x}, t)$ and assume that all the grains composing the material have a constant density ρ_g, so that the density field is

$$\rho(\boldsymbol{x}, t) = \rho_g \phi(\boldsymbol{x}, t).$$

The mass conservation equation can then be written in terms of the volume fraction field as:

$$\frac{\partial \phi}{\partial t} + \nabla \cdot (\phi \boldsymbol{u}) = 0. \tag{2.2}$$

The momentum conservation equation is

$$\rho \left(\frac{\partial \boldsymbol{u}}{\partial t} + (\boldsymbol{u} \cdot \nabla) \boldsymbol{u} \right) - \nabla \cdot \boldsymbol{\sigma} = \boldsymbol{f} \tag{2.3}$$

with $\boldsymbol{\sigma} \equiv \boldsymbol{\sigma}(\boldsymbol{x}, t)$ is the Cauchy stress tensor and $\boldsymbol{f}$ denotes the external volumic forces.

Note that the volume fraction field ϕ takes by definition values between 0 and some critical value ϕ_c, which accounts for the maximal "packing" fraction of the grains. As such, the granular material is not supposed uniformly dense, and the model can describe the different phases of granular matter. The varying volume fraction thus tightly couples the mass and momentum conservation equations (2.2) and (2.3) through the phase-dependent constitutive relation $\boldsymbol{\sigma}\,[\dot{\boldsymbol{\epsilon}}, \phi]$ required to close the system.

2.2. *The plastic Drucker-Prager rheology*

The central feature of granular materials is the existence of a pressure-dependent yield stress, somehow reminiscent of the Amontons-Coulomb law for solid friction. As mentioned above, we consider the material as perfectly plastic, following the Drucker-Prager rheology proposed in Drucker & Prager (1952). Note that our choice for such perfectly plastic modelling naturally allows to overcome the numerical stiffness inherent to the very small time scales resulting from granular elasticity. This is in contrast with the elasto-plastic models of Dunatunga & Kamrin (2015); Mast *et al.* (2015) or Klár *et al.* (2016), which are theoretically able to account for more complex physics but require in practice artificially lower elastic stiffnesses in order to ensure numerical workability, thereby weakening the physical meaning of elastic modelling for hard granular material.

Introducing the usual isotropic-deviatoric decomposition of tensors

$$\boldsymbol{\tau} = \frac{\mathrm{Tr}(\boldsymbol{\tau})}{d} \mathbb{I}_d + \mathrm{Dev}(\boldsymbol{\tau}),$$

where d is the dimension of the space, we assume that the *dense* state ($\phi = \phi_c$) is governed by the constitutive relation

$$\|\mathrm{Dev}\,(\boldsymbol{\sigma})\| \leqslant \mu p \qquad \text{if} \quad \mathrm{Dev}(\dot{\boldsymbol{\epsilon}}) = 0 \quad \text{(static regime)} \tag{2.4a}$$

$$\mathrm{Dev}\,(\boldsymbol{\sigma}) = \mu p \, \frac{\mathrm{Dev}\,(\dot{\boldsymbol{\epsilon}})}{\|\mathrm{Dev}\,(\dot{\boldsymbol{\epsilon}})\|} \qquad \text{if} \quad \mathrm{Dev}(\dot{\boldsymbol{\epsilon}}) \neq 0 \quad \text{(flowing regime)} \tag{2.4b}$$

where we have defined the pressure $p = -\frac{\mathrm{Tr}(\boldsymbol{\sigma})}{d}$ and the Frobenius tensor norm $\|\boldsymbol{\tau}\| \equiv \sqrt{\frac{\boldsymbol{\tau}:\boldsymbol{\tau}}{2}}$ associated to the natural inner product $\langle \boldsymbol{\tau}, \boldsymbol{\upsilon} \rangle = \frac{\boldsymbol{\tau}:\boldsymbol{\upsilon}}{2} = \frac{\mathrm{Tr}(\boldsymbol{\tau}^T \boldsymbol{\upsilon})}{2}$.

We also assume that for $\phi < \phi_c$, the material is in a *disconnected stress-free* state $\boldsymbol{\sigma} = 0$, as proposed in Narain *et al.* (2010) and Dunatunga & Kamrin (2015). In our case, this can be naturally imposed through the Drucker-Prager rheology by simply constraining the pressure

to vanish for $\phi < \phi_c$, which can be written concisely as a complementarity condition

$$0 \leqslant \phi_c - \phi \;\perp\; p \geqslant 0 \tag{2.5}$$

or equivalently $\phi \leqslant \phi_c$, $p \geqslant 0$ and $(\phi_c - \phi)\, p = 0$. When the volume fraction is below the packing fraction ϕ_c, the complementarity relation constrains the pressure to vanish, which imposes $\mathrm{Dev}\,(\boldsymbol{\sigma}) = 0$ and as a result $\boldsymbol{\sigma} = \mathrm{Dev}\,(\boldsymbol{\sigma}) - p\mathbb{I}_d = 0$.

The resulting constitutive relation is a constrained multi-valued and not everywhere differentiable functional. Solving for the whole system of equations (2.2) and (2.3) with (2.4*a*), (2.4*b*) and (2.5) is therefore numerically challenging, and is often handled through a regularisation of the rheology to reformulate the problem as a complex fluid as in Lagrée *et al.* (2011) or Franci & Cremonesi (2019), or solved using a full elasto-plastic model with explicit or implicit return-mapping projections as Dunatunga & Kamrin (2015); Mast *et al.* (2015); Klár *et al.* (2016).

The former approach suffers from viscous artifacts such as effective creeping flows, which can affect some physical observations. The latter approach is able to recover accurately the yield condition at the expense of small time-steps imposed by the small elastic time scale of hard granular material, thereby strongly increasing the computational costs, and intrinsically opposes recompaction after plastic expansion, leading to eventual volume gains.

One can also mention the approach of Ionescu *et al.* (2015) which is based on an augmented Lagrangian formulation to solve for the corresponding variational inequality, and could therefore in theory deal with the non-differentiability of the rheology but requires in practice a viscous regularisation to ensure viable convergence of the iterative fixed point algorithm.

In contrast, our numerical approach is entirely based on nonsmooth optimisation tools, and exploits in particular the similarities between the Drucker-Prager yield criterion and the Amontons-Coulomb friction law to leverage recent developments in the field of contact dynamics.

2.3. *Numerical method*

As mentioned above, our simulation framework is based on the 3D nonsmooth numerical model introduced in (Daviet & Bertails-Descoubes 2016*b*), which rewrites the plastic Drucker-Prager equations as a nonsmooth root-finding problem, and leverages efficient Gauss-Seidel algorithms originally developed in the context of *contact dynamics* (Moreau 1994; Jean 1999) to solve for the resulting non-linear equation. Details about this approach can be found in Daviet & Bertails-Descoubes (2016*b*,*a*), and are briefly described here for the sake of completeness.

Introducing the material derivative

$$\frac{D\bullet}{Dt} \equiv \frac{\partial \bullet}{\partial t} + \boldsymbol{u} \cdot \nabla \bullet\,,$$

we can rewrite the mass conservation equation (2.2) as

$$\frac{D\phi}{Dt} + \phi\, \nabla \cdot \boldsymbol{u} = 0,$$

which can be discretised in time with a first-order Euler scheme,

$$\phi^{(n+1)} = \phi^{(n)} - \delta t\, \phi^{(n)} \nabla \cdot \boldsymbol{u}, \tag{2.6}$$

where $\phi^{(n+1)} \equiv \phi(\boldsymbol{x}(t+\delta t), t+\delta t)$ and $\phi^{(n)} \equiv \phi(\boldsymbol{x}(t), t) = \phi(t)$. This allows us to linearise the complementarity relation (2.5) by enforcing the $\phi \leqslant \phi_c$ constraint on the Lagrangian

transported volume fraction, namely

$$0 \leqslant \phi(t)\nabla\cdot\boldsymbol{u} + \frac{\phi_c - \phi(t)}{\delta t} \;\perp\; p \geqslant 0,$$

which is now linear in $\boldsymbol{u}$.

Defining the auxiliary tensor fields

$$\boldsymbol{\lambda} \equiv -\boldsymbol{\sigma}$$
$$\boldsymbol{\gamma} \equiv \phi(t)\,\dot{\boldsymbol{\epsilon}} + \frac{\phi_c - \phi(t)}{d\,\delta t},$$

the whole rheology can be written as

$$\mathcal{DP}(\mu) \equiv \begin{cases} \|\mathrm{Dev}\,(\boldsymbol{\lambda})\| \leqslant \mu\,\dfrac{\mathrm{Tr}\,(\boldsymbol{\lambda})}{d} & \text{if} \quad \mathrm{Dev}(\boldsymbol{\gamma}) = 0 \quad \text{(static regime)} \\ \mathrm{Dev}\,(\boldsymbol{\lambda}) = -\mu\,\dfrac{\mathrm{Tr}\,(\boldsymbol{\lambda})}{d}\,\dfrac{\mathrm{Dev}\,(\boldsymbol{\gamma})}{\|\mathrm{Dev}\,(\boldsymbol{\gamma})\|} & \text{if} \quad \mathrm{Dev}(\boldsymbol{\gamma}) \neq 0 \quad \text{(flowing regime)} \\ 0 \leqslant \mathrm{Tr}\,(\boldsymbol{\gamma}) \;\perp\; \mathrm{Tr}\,(\boldsymbol{\lambda}) \geqslant 0. \end{cases} \tag{2.7}$$

As shown in (Daviet & Bertails-Descoubes 2016*b*,*a*), this rheological law can be recast as a normal cone inclusion in $\mathbb{R}^{s(d)}$ with $s(d) \equiv \frac{d(d+1)}{2}$ the dimension of $S(d)$ the space of symmetric $d \times d$ matrices. It is thus equivalent to a root-finding problem on a generalised Fischer-Burmeister non-smooth function introduced in (Fukushima *et al.* 2002) and modified in (Daviet *et al.* 2011) to handle non-symmetric and non-associated second-order cone complementarity problems. We denote here f_{MFB} this modified Fischer-Burmeister function. Additional details regarding the definition of f_{MFB} is given in appendix A.1. We then have

$$(\boldsymbol{\gamma}, \boldsymbol{\lambda}) \in \mathcal{DP}(\mu) \iff f_{\mathrm{MFB}}(\boldsymbol{\gamma}, \boldsymbol{\lambda}) = 0. \tag{2.8}$$

The conservation equations are then discretised in space using an hybrid Finite-Element/Material-Point Method (FEM-MPM) described in appendix A.2, finally giving the algebraic problem

$$\text{Find } \boldsymbol{\gamma}, \boldsymbol{\lambda} \in S(d) \times S(d) \text{ s.t.} \quad \begin{cases} \boldsymbol{\gamma} = \boldsymbol{W}\boldsymbol{\lambda} + \boldsymbol{b} \\ (\boldsymbol{\gamma}, \boldsymbol{\lambda}) \in \mathcal{DP}(\mu), \end{cases} \tag{2.9}$$

which is solved by minimising the functional

$$\mathcal{F}[\boldsymbol{\lambda}] \equiv \frac{1}{2}\|f_{\mathrm{MFB}}(\boldsymbol{W}\boldsymbol{\lambda} + \boldsymbol{b}, \boldsymbol{\lambda})\|^2 \tag{2.10}$$

using a Gauss-Seidel iterative procedure with a generalised Newton algorithm to solve the local problems. The overall algorithm is summarised in appendix A.3.

Note that the constraint $(\boldsymbol{\gamma}, \boldsymbol{\lambda}) \in \mathcal{DP}(\mu)$ in equation (2.9) actually denotes a vector concatenation of local constraints: for each finite-element interpolation node $\boldsymbol{x}_i$, we require that the local auxiliary stress and strain rate tensors satisfy the Drucker-Prager yield constraint, i.e. $\forall i, (\boldsymbol{\gamma}(\boldsymbol{x}_i), \boldsymbol{\lambda}(\boldsymbol{x}_i)) \in \mathcal{DP}(\mu)$. The yield constraint is thus only imposed strongly at interpolation points, but not at the continuous nor integral level. In practice, due to the strong non-linearity of the constraint and the MPM interpolation, this can induce small but noticeable constraint violations, which manifest themselves in particular as potential volume losses over the course of long simulations (note that the *mass* is however accurately conserved as imposed by equation (2.2)). In the following simulations, we have carefully adjusted the numerical parameters to ensure that the total relative volume losses always stay below 3%.

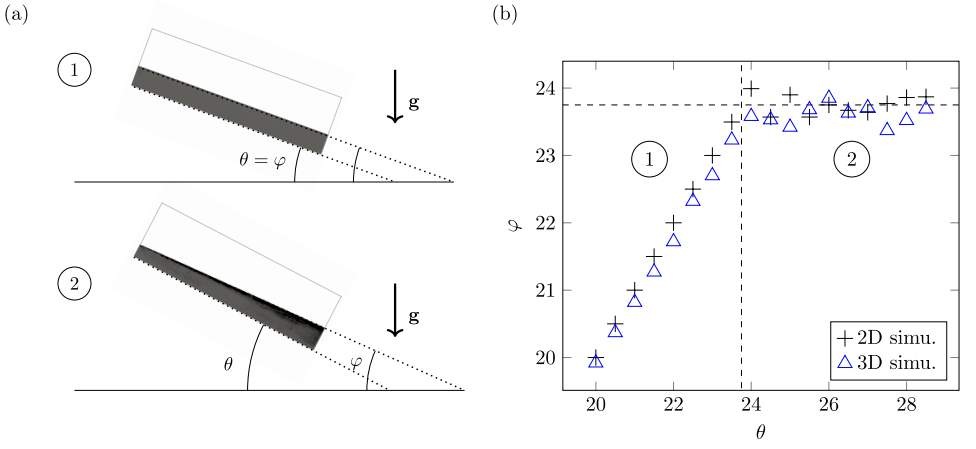

Figure 1: Inclination φ of the stabilised granular bed free surface as a function of the box inclination θ for the avalanche numerical setup obtained in our 2D and 3D simulations. (a) Simulation snapshots of the 2D granular bed for $\theta = 23°$ and $27°$. (b) φ vs θ, the vertical and horizontal dashed lines indicate the friction angle used in the simulation $\tan^{-1}(0.44) \approx 23.75°$.

2.4. *Drucker-Prager friction coefficient and yield transition*

As shown above, our model solves for a perfectly plastic Drucker-Prager rheology, without regularising the yield criterion. As such, it features a *single* friction coefficient μ which defines the yield surface, and thereby the transition between the static and flowing regimes.

To assess the numerical behaviour of our model close to the yield point, we consider a simple avalanche experiment: a two- or three-dimensional dense bed of granular material with height h in a closed box under gravity is quasi-statically inclined, and we measure for each bed inclination θ the corresponding stabilised granular free-surface φ.

This simple "inclined chute" configuration usually involves two characteristic angles: the *start* – or *avalanche* angle θ_a, which is the maximal possible angle attainable with a static granular bed, and the *stop* angle θ_s, which is the minimal angle needed to sustain flow in the same granular bed (c.f. Daerr & Douady (1999); Savage (1979); Pouliquen & Forterre (2002); Artoni *et al.* (2011)). In our model however, we only parameterise the yield transition using a *single* friction coefficient. As such, we do not expect to recover the full hysteretic phenomenology of such experiments, but rather seek to characterise our Drucker-Prager rheology from a macroscopic point of view, and to provide a way to set the friction coefficient μ in the context of granular collapses.

We consider in practice a 2D (or 3D) box of dimensions $1\,\text{m} \times 0.3\,\text{m}$ ($\times 0.1\,\text{m}$), discretised with a cartesian mesh with resolution 250×150 (resp. $100 \times 30 \times 10$), filled with a 0.1 m-high bed of granular material with slip boundary conditions on the sides and stick boundary conditions at the bottom of the box. To minimise the effect of boundary conditions, we measure the angle of the free surface between $x = 0.3\,\text{m}$ and $0.7\,\text{m}$ using a $\tan^{-1}$ on the end-point coordinates of a line fit. The simulation time-step is chosen as $\delta t = 1\,\text{ms}$ and we increase θ by steps of $0.5°$ ensuring equilibrium is always reached between each change of inclination. Note that the simulated box is actually kept fixed and we vary the inclination θ by rotating the external gravity force.

Figure 1 shows the results for the free surface angle φ, once the surface has stabilised, as a function of θ for a simulation with $\mu = 0.44$. As we increase the bed inclination θ, we observe

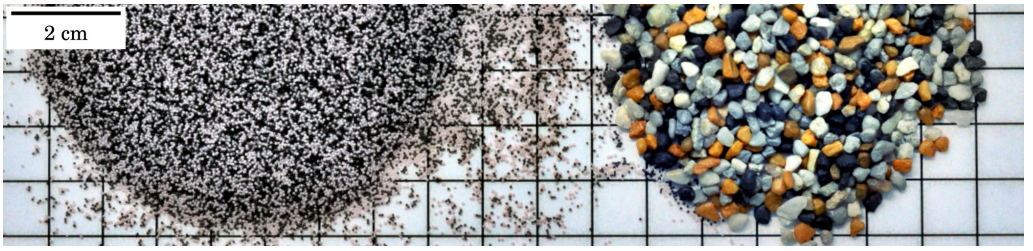

Figure 2: Photograph of the two granular materials used for our validation experiments: glass beads on the left, and natural irregular granules on the right. Multicoloured material improves feature detection, hence velocimetry performance.

that the free surface first remains aligned with the bed ($\varphi = \theta$); the material is jammed and remains in static equilibrium. After some critical inclination θ_a (the so-called *avalanche* angle), the material starts to flow before stopping. If we again increase quasi-statically the bed inclination, the same happens again, and the angle of the stabilised free surface basically takes a constant value, corresponding to the so-called *stop* angle $\varphi_s = \theta_s$ for $\theta > \theta_a$.

As expected from our simple non-hysteretic Drucker-Prager model, we observe that the avalanche and stop angles are indistinguishable. Furthermore, as shown in figure 1 (b), both angles correspond precisely to the friction angle prescribed by the friction coefficient μ of the Drucker-Prager law, as $\theta_a = \theta_s = \theta_\mu = \tan^{-1}(\mu)$.

On the one hand, these two observations demonstrate that our numerical model provides a consistent discretisation of the Drucker-Prager law, and gives us confidence in using the corresponding Sand6 code for further experiments. On the other hand, this elementary numerical experiment makes it clear that modelling granular material with a simple plastic Drucker-Prager rheology requires to be careful in the choice of the – constant – friction coefficient.

In the following, we show that our numerical model, which features a single friction parameter, is sufficient to predict the macroscopic flowing of a real granular collapse, provided the friction coefficient is chosen as the *avalanche* angle θ_a of the real granular material. This observation, which departs from the usual choice for setting the friction parameter (the stop angle), is supported by complementary validations and comparisons of our model throughout the paper, and eventually discussed.

3. Experimental collapses and measure of macroscopic parameters

In order to validate our nonsmooth simulator in transient flow configurations, we have conducted various experiments of granular column collapses in a 6 cm-wide channel. Our experiments are performed on various inclinations of the channel bed and using two different materials, which we describe in the following. To relate our physical experiments to our numerical simulations, we also need to measure appropriately, from the experiments, all the – macroscopic – parameters at play in the continuum model: in particular the yield friction coefficient μ of the Drucker-Prager rheology, but also the friction coefficient between the granular medium and the lateral walls. These measurement processes are discussed in this section.

3.1. *Materials*

We consider two different materials: 0.5 mm glass beads (Sigmund Linder - SiliBeads - 45015) and 2.7 mm natural granules. Their aspects are shown in figure 2, and their physical parameters – which we have experimentally measured – are summarised in table 1.

type	d (mm)	ρ_c (kg m^{-3})	μ_a	μ_s	μ_w
glass beads (B)	0.5	1.47×10^3	0.44 ± 0.03	0.37 ± 0.03	0.23 ± 0.05
granules (G)	2.7	1.52×10^3	0.75 ± 0.1	0.65 ± 0.1	0.3 ± 0.1

Table 1: Measured material and rheological parameters for the two granular materials used in our experiments: d is the median grain diameter, ρ_c the density of the material in the dense state, μ_a the avalanche friction coefficient, μ_s the stop friction coefficient, and μ_w the estimated friction coefficient between the granular material and the lateral walls. Note that the density ρ_c is measured on the granular media in its dense state and not on the composing grain, and corresponds as such to a direct measurement of $\rho_c = \rho_g \phi_c$.

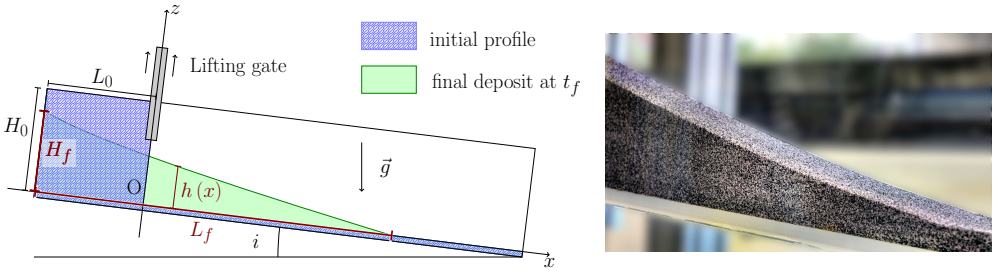

Figure 3: [left] Sketch of our granular column-collapse experimental configuration showing the initial column dimension (L_0,H_0) and final deposit state (run-out L_f and final upslope height H_f). Collapses are triggered by a pneumatic lifting gate. [right] Photograph of the final deposit.

Our 0.5 mm glass beads share the same geometric and physical features as the glass beads used in (Pouliquen 1999; Pouliquen & Forterre 2002; Jop *et al.* 2005). The latter references represent seminal experimental works for calibrating the $\mu(I)$ constitutive law of Jop *et al.* (2006), relying on a steady granular flow in a wide channel with various inclinations. In section 3.3, we verify experimentally that our beads behave in accordance with the results reported in the aforementioned literature, when subjected to a similar setting. We note that our beads are also similar to those used for the granular collapses studied in Mangeney-Castelnau *et al.* (2005); Farin *et al.* (2014), whose experimental results are exploited to test modelling assumptions formulated by Ionescu *et al.* (2015) and later by Martin *et al.* (2017). Aligning our choice on this material thus makes it possible to check such assumptions and better transfer insights. For this reason we have used this well-calibrated model material preferably for extensive and systematic validation, as reported in section 4.2.

In order to test the robustness of our model on natural materials – generally exhibiting larger friction coefficients than spherical glass beads, we have also used coarse natural granules (2.7 mm irregular grains). The extension of our validation study to the collapse of such natural granules is provided in section 4.3.

3.2. *Collapse set-up*

The experimental apparatus is inspired by Balmforth & Kerswell (2005) and sketched in figure 3. An initial granular pile with aspect ratio $a = H_0/L_0 \sim 0.5$, where H_0 is the depth and L_0 is the length along the channel, is confined in a $W = 6$ cm wide flume with a lifting gate preventing the pile to collapse. The experiment consists in opening the pneumatic lifting

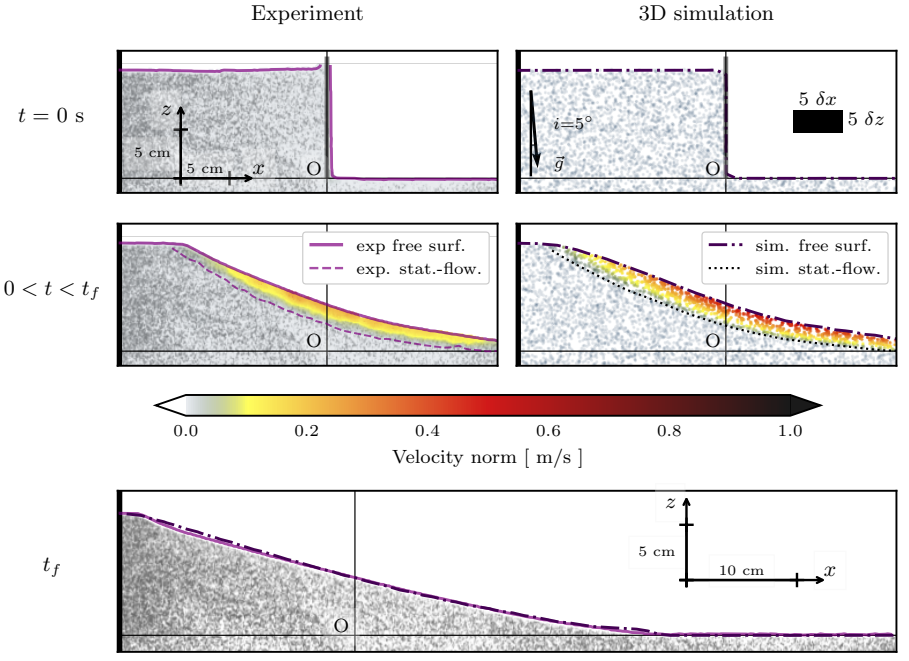

Figure 4: Capturing the free surface and velocity field from experimental and simulated granular collapses at different instants. Camera snapshots are shown in left column and bottom figures where experimental velocities are extracted using image velocimetry and shown on the snapshots foreground. The static-flowing transition corresponds to the 0.01 m/s contour of the experimental and numerical velocity fields. The simulated material points are shown on the right column and coloured according to their velocity magnitude. The black rectangle on the top left figure has dimensions $5\,\delta_x \times 5\,\delta_z$ with δ_x and δ_z the respective horizontal and vertical MPM resolutions. Data correspond to the B05 collapse (0.5 mm beads – $i = 5°$). See movie 1 in the online supplementary material for a visualisation of the experimental and simulated evolution in time.

gate to trigger the granular collapse. Similarly to the second set of experiments of Farin *et al.* (2014), the base of the box is covered with an horizontal erodible granular bed of ~ 2 cm height made of the same material.

Free surface profiles as well as velocities are collected using a high-speed camera from the transparent side walls with an interframing time of 5.3 ms. We estimate the local optical flow of good feature to track (Shi 1994; Miozzi *et al.* 2008), i.e. features having optimal contrasts to be tracked (enhanced by the presence of multicoloured materials as shown in figure 2). We interpolate feature velocities on a mesh to produce the velocity fields using the *opyf* python package. The reader may refer to Annex 1 of Rousseau & Ancey (2020) for details on the velocimetry procedure.

Figure 4 illustrates the methodological data used to compare experiments and simulations in this article: the upper left column shows snapshots of the recorded experimental collapse for the initial and some intermediate state, coloured with the velocity magnitude as measured by velocimetry, while the upper right column shows the corresponding snapshots of the simulation, where the background medium and velocity are displayed by the Material Points quantities. We superpose on all these snapshots the post-processed profile height and static-flowing transition lines, respectively determined as the 0.5 contour on the volume fraction ϕ

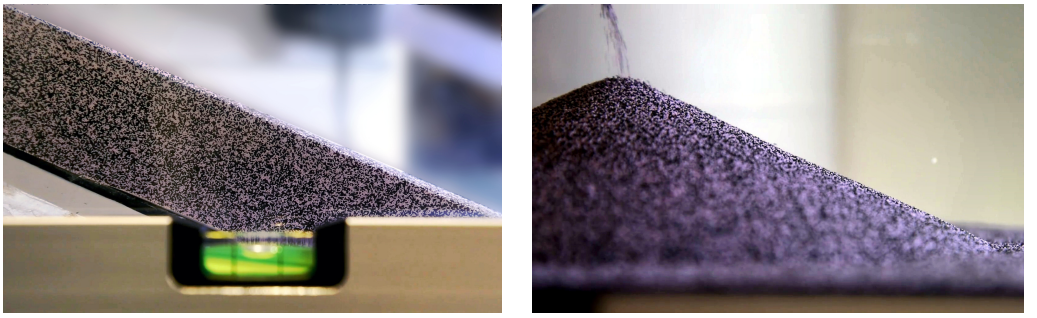

Figure 5: The avalanche angle θ_a, used to set the yield friction coefficient μ of the Drucker-Prager model as $\mu = \mu_a = \tan\theta_a$ using either the large channel inclination test (left), or the conical heap test (right). For our 0.5 mm glass beads depicted here, both protocols converged to a same average measurement value ($\tan\theta_a = \tan 23.7^\circ = 0.44 \pm 0.03$)

and 0.01 m/s contour on the velocity. The bottom figure illustrates the direct comparison of the height profiles in the final state.

3.3. *Measurement of macroscopic parameters*

As mentioned in section 2.4, the flowing threshold in our Drucker-Prager constitutive law is determined by a single friction coefficient $\mu = \tan\theta$. Yet, there is still no clear consensus regarding which of the avalanche angle θ_a and the stop angle θ_s should be used as the yield angle. In order to discriminate between these two options, we first need to measure both parameters for the granular media used in our experiments. Since the role of sidewalls is also investigated, we furthermore evaluate the friction coefficient between the granular medium and the lateral walls μ_w.

3.3.1. *Measurement of the avalanche friction coefficient*

Our first experiment for measuring the avalanche angle θ_a, is based on the configuration used by Balmforth & Kerswell (2005) for measuring the "internal" angle of friction – a terminology which is then equivalent to our avalanche angle from an experimental point of view. Similarly to the numerical set-up presented in section 2.4, we consider a 20 cm wide flume filled with the granular material and incline the flat granular bed until motion downslope begins (see figure 5, left). Our second experiment consists in pouring slowly granular material upon a conical heap (see figure 5, right). In both experiments, we measure θ_a as the critical angle corresponding to the maximal slope of the material, just before an avalanche occurs and causes the slope to decrease (see movie 2 in the online supplementary material for an illustration of the process). As emphasised by Balmforth & Kerswell (2005) or Russell *et al.* (2019), there is a large spread in the θ_a measurements owing to the sensitivity of the protocol to small perturbations.

For the 0.5 mm glass beads material, no matter the experimental protocol used (inclined channel or conical heap), we found the avalanche angle $\theta_a = 23.7^\circ \pm 1$, which corresponds to the friction coefficient $\mu_a = \tan\theta_a \approx 0.44 \pm 0.03$. This value is consistent with those made in the literature for similar materials, such as the 0.7 mm or 0.8 mm glass beads of respectively Farin *et al.* (2014) and Balmforth & Kerswell (2005) which give $\tan\theta_a = \tan 25^\circ = 0.47 \pm 0.01$ and $\tan\theta_a = \tan 24.5^\circ = 0.46 \pm 0.04$. For the 2.7 mm granules, we have only conducted the experiment with the first protocol, and found $\theta_a = 36.8^\circ \pm 5$ ($\mu_a = 0.75 \pm 0.1$).

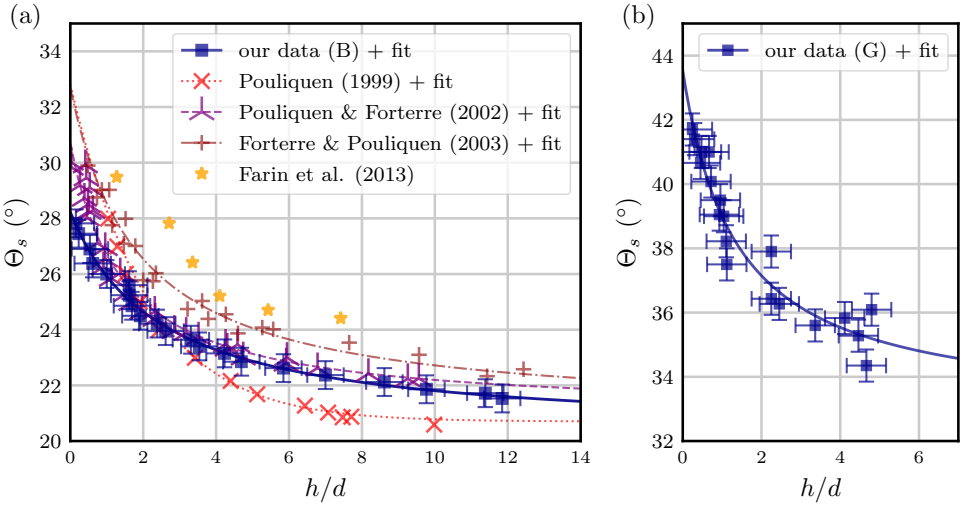

Figure 6: (a) Variation of the stop angles Θ_s as a function of the non-dimensional thickness h/d for our glass beads (B) of diameter $d = 0.5$ mm, measured using the protocol described in Pouliquen & Forterre (2002). The plain curve corresponds to the best fit of our data with the function $\tan(\Theta_s(h)) = \mu_1 + (\mu_2 - \mu_1)/(1 + h/L)$, obtained for $\mu_1 = 0.37$, $\mu_2 = 0.54$ and $L = 1.16$ mm. We also report the data and fits of Pouliquen & Forterre (2002), Pouliquen (1999), Forterre & Pouliquen (2003) and Farin *et al.* (2014) for the sake of comparison. Curves do not all collapse perfectly, which may be explained by slight differences between experimental conditions, protocols or materials. Overall, our data look consistent with the previous studies performed with 0.5 mm glass beads. (b) Same measurements made for our granules (G) with a best fit obtained for $\mu_1 = 0.65$, $\mu_2 = 0.95$ and $L = 3.1$ mm.

3.3.2. *Measurement of the stop friction coefficient*

As mentioned above, another feature of granular flows is the existence of a minimal angle necessary to sustain motion in an already flowing material. In the case of a granular layer with constant height flowing on rough inclines, this *stop* angle depends on the height h as a function $\Theta(h)$ (Pouliquen 1999; Pouliquen & Forterre 2002), which naturally converges toward a constant value as the height increases, namely $\theta_s = \Theta_s(h \to \infty)$.

This phenomenology has led to nowadays well-established protocols to measure θ_s in a steady granular flow, in which either the bed with steady flow of known height is progressively lowered until flow ceases (Pouliquen 1999), or the initially static bed is inclined up until it starts to flow, and then stops (Pouliquen & Forterre 2002).

We have replicated the steady inclined bed protocol experimentally with our 0.5 mm beads and 2.7 mm granules, and have measured the resulting stop angle as in Pouliquen & Forterre (2002) using a 3 m-long, 10 cm-wide channel ($W/d = 200$) for beads and a 2 m-long, 12 cm-wide channel for granules ($W/d = 44$).

While our channels are narrower than the one used in Pouliquen & Forterre (2002), the maximal characteristic flowing heights h are systematically small w.r.t the channel W, with $h/W \sim 0.06$ for both beads and granules. Following Jop *et al.* (2005), side wall friction can thus result in a small overestimation of the stop friction coefficient of order $\mu_w h/W \sim 0.02$ in both cases.

Our results for beads are shown in figure 6 (a), together with the experimental data and corresponding fits of Pouliquen (1999); Pouliquen & Forterre (2002); Forterre & Pouliquen

(2003); Farin *et al.* (2014). We observe that despite some spreading in all the collected data, which might be attributed to the different experimental protocols used – Pouliquen & Forterre (2002) vs. Pouliquen (1999) – and/or to the slightly different beads used – Pouliquen & Forterre (2002) vs. Farin *et al.* (2014) –, we obtain a good agreement with Pouliquen & Forterre (2002), in particular regarding the $h/d_p \rightarrow +\infty$ asymptote, which corresponds to the $I \rightarrow 0$ stop angle.

Indeed, we retrieve a stop friction coefficient $\mu_s = \tan(\Theta_s(\infty)) = \mu_1 = 0.37$ which is very close to the values for the same type of beads, $\mu_s = 0.38$ (Pouliquen 1999; Pouliquen & Forterre 2002; Jop *et al.* 2006). Accounting for the 10 cm width of our channel, we thus deduce that our actual stop friction coefficient is slightly less than 0.37. In practice, for our comparisons we shall stick to $\mu_s = 0.38$ (see section 4.4).

Following the same measurement protocol with our granules, we find a stop friction coefficient of $\mu_s = 0.65 \pm 0.1$ for this natural sediment (see table 1 and figure 6 (b)).

These results confirm that our beads behave fairly similarly to the ones from Pouliquen & Forterre (2002), which enables direct comparison of our results with other works.

It is noteworthy that whatever the material used, the estimated stop friction coefficient ($\mu_s = 0.38$ and $\mu_s = 0.65$ for the beads and granules, respectively) is significantly lower compared to the measured avalanche coefficient ($\mu_a = 0.44$ and $\mu_a = 0.75$ respectively). In section 4, we find that using $\mu = \mu_a$ in our simulations yields more realistic collapses than taking $\mu = \mu_s$.

3.3.3. *Measurement of the friction coefficient between the granular medium and the lateral walls*

Following Balmforth & Kerswell (2005); Hutter & Koch (1991), we estimate the friction coefficient μ_w between the glass walls and the granular materials by measuring the critical angle above which a block of particles held together within a rigid light plastic cylinder begins to slide on an inclined glass surface. The cylinder is 4 cm in diameter and 6 cm high. We obtain $\mu_w = \tan(13°) = 0.23$ for the 0.5 mm glass beads and $\mu_w = \tan(17°) = 0.3$ for the 2.7 mm granules. These values are reported in table 1 along with the corresponding estimated standard deviations.

4. Validation: numerics vs. experiments

To evaluate the performance of our simulation approach and assess the validity of the Drucker-Prager rheological law – featuring only one friction coefficient – in the case of transient collapse flows, we perform direct 3D simulations of the collapse setups presented in section 3.2, with full account of frictional interactions with the encasing walls and the lifting door.

We first compare the simulation results with the experiments for the glass beads (B), in order to validate our numerical model with a controlled material, and then highlight its robustness by considering the case of natural irregular granules (G) (c.f. figure 2).

4.1. *Simulation parameters*

The rheological parameters used in our simulations are derived from independent experimental measurements performed with the same materials. As discussed in section 3.3.1, the Drucker-Prager friction coefficients are determined using the respective avalanche angles, measured consistently with both the channel and heap setups. To reduce uncertainties on the actual granular dense packing fraction, the density is directly measured for the granular media in the dense state, and thus corresponds to the critical density $\rho_c = \rho_g \phi_c$. This amounts to rescaling the volume fraction field ϕ by its dense critical value ϕ_c, so as to ensure

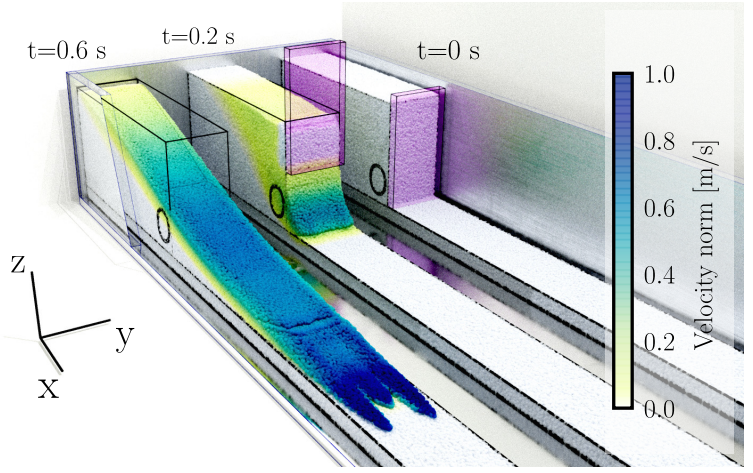

Figure 7: 3D MPM simulations of the B15 granular column collapses over a 15°-tilted bed at three different times. The motion due to the lifting gate is particularly visible at $t = 0.2$ s. A three-dimensional animated visualisation is provided in the online supplementary material (c.f. movie 3).

$\rho_c \frac{\phi}{\phi_c} = \rho_g \phi = \rho$. As such, we take in the simulations $\phi_c = 1$. The values for the material parameters and the friction coefficients are summarised in table 1.

Gravity is set to its standard value $g = 9.81\,\mathrm{m\,s^{-2}}$, and aligned with a rotated downward unit vector to account for the various respective inclinations of the collapse beds.

The $152 \times 15 \times 6\,\mathrm{cm}^3$ simulation domain is discretised with a $152 \times 30 \times 6$ mesh of regular rectangular cuboids, which gives a 1 cm length and width resolution, and a 0.5 cm resolution for the height, in order to better capture the free surface. Top right plot in figure 4 illustrates the resolution of the background MPM-grid: the black rectangle has dimensions $5\,\delta_x \times 5\,\delta_z$ where δ_x and δ_z are the horizontal and vertical resolutions respectively.

We impose frictional boundary conditions with the lateral walls and the left upstream wall – the bottom wall being covered with a 2 cm bed of erodible granular material to ensure the same bulk friction conditions. As mentioned in section 3.2, the experimental collapses are initiated by the lifting of a pneumatic gate, which can interact frictionally with the granular material and affect the flow in the initial phase. We therefore directly account for the lifting of the gate by introducing a rigid plane with imposed motion mimicking the gate. This "numerical" door also interacts frictionally with the material, with the same friction coefficient μ_w as the lateral walls. Figure 7 illustrates the numerical setup with the lifting of the gate. Note that while the upward lifting motion of the door influences the early dynamics and the final state of the collapse, frictional interaction between the material and the door plays a negligible role on the flow, as discussed in appendix B.2.

The simulations are run with about 216 MPM particles per mesh cell, with random initial positions, and a time-step of 8.3×10^{-4} s.

4.2. *Validation on glass beads at various inclinations*

Figure 8 shows a comparison between the mid-width profiles for the collapse experiments and simulations performed on our 0.5 mm glass beads for 5 bed inclinations, ranging from 0° to 20°. The profiles are plotted at three different times, to highlight the behaviour of the collapse in the starting, flowing and stopped phases. The right-most column shows the final state of the deposit, when the mass has stopped moving, i.e. when we detect no velocity above 0.01 m/s in the whole domain, with corresponding respective experimental and simulation

Run	B00	B05	B10	B15	B20	G00	G05	G10	G15
i (°)	0	5	10	15	20	0	5	10	15
$t_{f,\text{exp}}$ (s)	0.99	1.23	1.63	1.72	2.79	.79	0.89	0.99	1.09
$t_{f,\text{sim}}$ (s)	0.87	1.00	1.30	1.47	2.10	0.47	0.53	0.6	0.73
H_0 (m)	0.11	0.11	0.11	0.11	0.11	0.11	0.12	0.12	0.12
a	0.5	0.5	0.5	0.5	0.5	0.6	0.6	0.4	0.4
$H_{f,\text{exp}}$ (m)	0.11	0.11	0.09	0.07	0.04	0.12	0.12	0.12	0.12
$H_{f,\text{sim}}$ (m)	0.11	0.11	0.09	0.07	0.04	0.11	0.12	0.12	0.12
$L_{f,\text{exp}} - L_0$ (m)	0.18	0.22	0.31	0.49	-	0.11	0.15	0.10	0.24
$L_{f,\text{sim}} - L_0$ (m)	0.19	0.21	0.30	0.46	0.88	0.10	0.13	0.15	0.19

Table 2: Metrics of the experimental and numerical runs. The letter B indicates glass bead material and G indicates granules. The experimental and simulation rest times ($t_{f,\text{exp}}$ and $t_{f,\text{sim}}$) correspond to the times when we detect no velocity above 0.01 m/s in the domain. H_0 is the initial pile height and a the initial collapse aspect ratio. $H_{f,\text{exp}}$ and $H_{f,\text{sim}}$ are the experimental and simulated final pile height while $L_{f,\text{exp}} - L_0$ and $L_{f,\text{mod}} - L_0$ are the experimental and simulated run-out distances measured from the gate position (L_f is defined as the run-out distance from the left collapse wall). Note that the missing final experimental run-out distance for the B20 collapse is due to restrictions on the field of view of the camera.

final – stop – times $t_{f,exp}$ and $t_{f,sim}$ which naturally depends on the bed inclination, as summarised in table 2. Note that the differences observed for the final time t_f between the experiment and the simulation are mainly caused by the local nature of the "rest" criterion we use (no velocity above 0.01 m/s in the whole domain), which artificially delays the final time of the experiment due to marginal grain movement at the free surface. We also plot the experimental and simulation static-flowing transition lines determined as the 0.01 m/s contour of the velocity field in order to highlight the bulk dynamics of the collapse.

We first observe an excellent agreement between the experimental and computed final thickness profiles for all the inclinations, highlighting the ability of our numerical method to capture threshold effects and large strains. The $t = 0.2$ s snapshots also highlight the important role of simulating the lifting of the door, which influences the initial dynamics, as also observed by Ionescu *et al.* (2015).

The dynamics of the collapses at early steps also appears to be well described by the simulation for small inclinations. Above 15° inclination, we observe some difference in the thickness profiles, with in particular a systematic under-estimation of the profile height near the left wall, which was also observed by Martin *et al.* (2017). The static-flowing transition lines follow the same overall behaviour, with a fair agreement for small inclinations, degrading for larger ones.

We also show the position and velocity of the granular front as a function of time in figure 9. We can first observe that our simulations accurately capture the stopping time of the front, with a rather good prediction of the front velocity for each collapse inclination. Note that the front always stops before the final stopping time t_f of the whole flow.

Overall, while the early dynamics of the collapses seem to depend on the inclination, these results validate our simulation approach, and in particular support the use of a simple Drucker-Prager law with the constant avalanche friction coefficient to capture final deposit profiles.

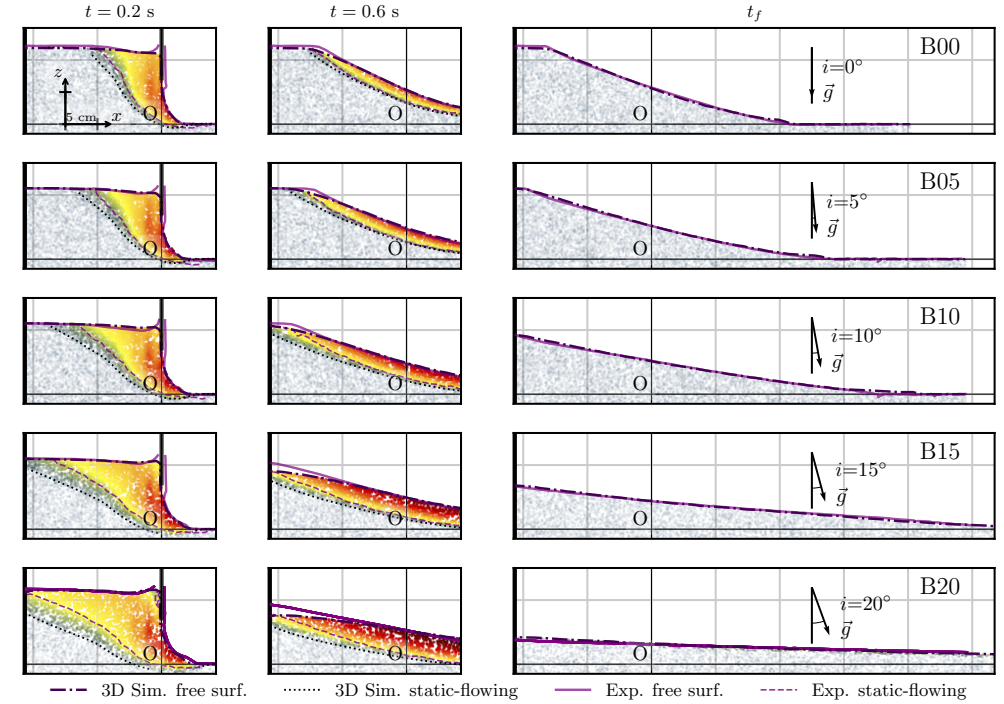

Figure 8: Comparison between collapse experiments with the 0.5 mm glass beads and 3D simulations for various bed inclinations ranging from 0° (top) to 20° (bottom) (B00, B05, B10 and B15 runs). The profiles are extracted at mid-width of the lateral walls. We compare both the thickness profiles (solid pink line for the experiment, dash-dotted black line for the simulation) and the static-flowing transition (pink dashed line for the experiment, black dotted line for the simulation). The velocity heatmap in the background is computed from the simulation. In the simulations, the constant friction μ was set to $\mu_a = 0.44$, and the wall friction to $\mu_w = 0.23$.

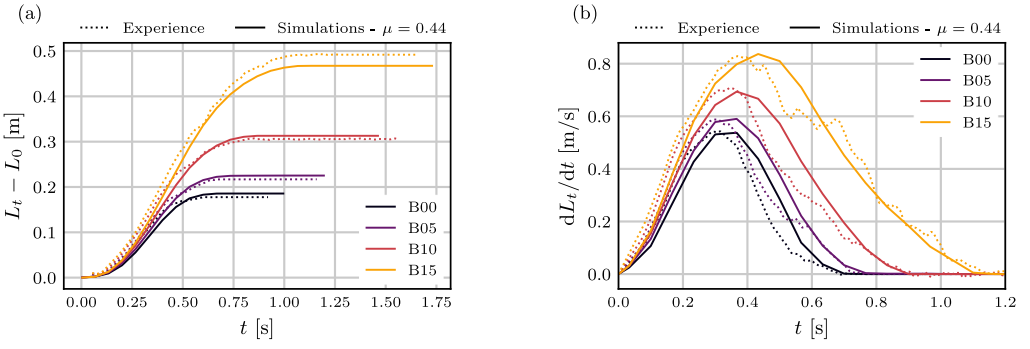

Figure 9: Front position (a) and velocity (b) for the experimental and simulated granular collapses, for bed inclinations from 0° (top) to 15°. Note that the run at 20° inclination was left out since our experimental recording setup could not frame the run-out during the whole collapse. The 3D simulations were performed with the constant friction $\mu = 0.44$, and the wall friction $\mu_w = 0.23$.

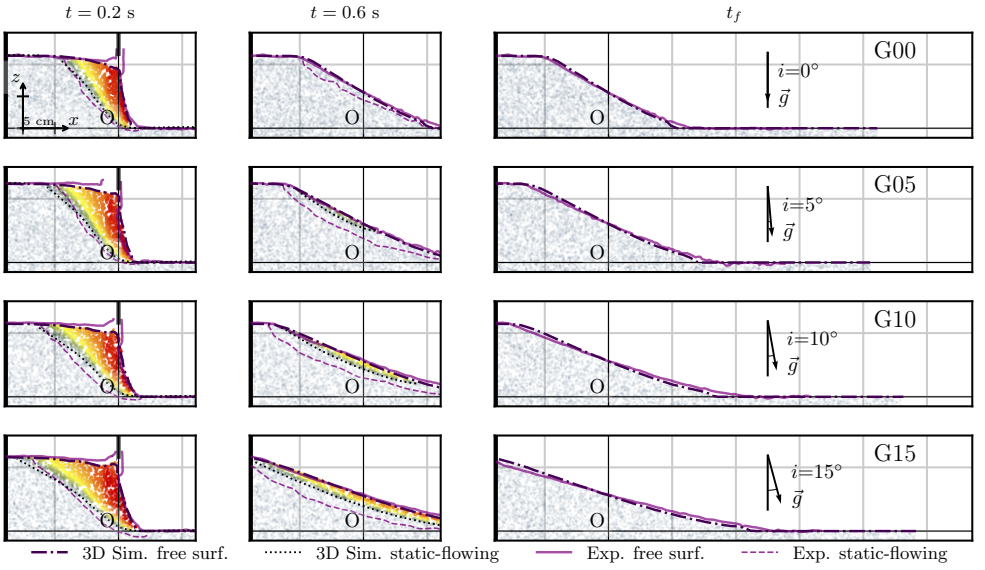

Figure 10: Comparison between collapse experiments with the natural granules and 3D simulations for various bed inclinations ranging from 0° (top) to 15° (bottom) (G00, G05, G10 and G15 runs). The profiles are extracted at mid-width of the lateral walls. We compare both the thickness profiles (solid pink line for the experiment, dash-dotted black line for the simulation) and the static-flowing transition (pink dashed line for the experiment, black dotted line for the simulation). The velocity heatmap in the background is computed from the simulation. In the simulations, the constant friction μ was set to $\mu_a = 0.75$, and the wall friction to $\mu_w = 0.3$. See movie 4 in the online supplementary material for an animated evolution of the G15 simulated collapse against experiment.

4.3. *Robustness: extension of prediction to other materials*

To illustrate the robustness of the Drucker-Prager rheology with the constant – avalanche – friction coefficient in predicting collapse flows, we perform similar experiments and simulations using a more natural and irregular material (denoted *granules* above, c.f. figure 2, table 1). The corresponding profiles are presented in figure 10. We again observe a good agreement between the experiments and simulations.

The small discrepancies observed close to the lifting gate at the beginning of the flow suggest that the frictional interaction of the material with the door is higher. We also notice, as was also the case for the glass beads, that the material flows less in the early dynamics, suggesting that more subtle rheological effects are at play in this stage. However, again this does not impact the final run-outs and profiles.

We should stress that the measurement protocols for the avalanche and stop friction coefficients are subjected to important uncertainties (as reported in table 1) in the case of such gritty material, due to the inherently large inclination angles required to reach the yield and stop transitions, and to the increased impact of boundary effects in the resulting very inclined channels. As such, we do not try to discriminate accurately against the use of either the avalanche or stop friction coefficient, but rather interestingly illustrate the reliability of the plain Drucker-Prager rheology in the context of transient collapse flows of natural materials.

4.4. *Comparison with the $\mu(I)$ rheology*

The $\mu(I)$ rheology, initially proposed by Jop *et al.* (2006) in the context of steady inertial flows, introduces a local dependence of the Drucker-Prager coefficient on the inertial number

$$I = \frac{d\|\dot{\epsilon}\|}{\sqrt{p/\rho}} \tag{4.1}$$

with d the particle diameter, $\dot{\epsilon}$ the strain-rate tensor introduced in equation (2.1), p the pressure and ρ the material density. This inertial number characterises the ratio between the inertial timescale $d\sqrt{\rho/p}$ and the deformation timescale $1/\|\dot{\epsilon}\|$.

The $\mu(I)$ rheology then writes

$$\mu(I) = \mu_s + \frac{\mu_2 - \mu_s}{1 + \frac{I_0}{I}} \tag{4.2}$$

where μ_s, μ_2 and I_0 are material-dependent coefficients which can be calibrated using the steady inclined plane experiment as described in Jop *et al.* (2005).

This model has recently been used with success for transient collapse prediction in several studies (Lagrée *et al.* 2011; Ionescu *et al.* 2015; Martin *et al.* 2017).

The $\mu(I)$ rheology equation (4.2) can be straightforwardly implemented in our simulation framework by adding an explicit friction coefficient update in the yield criterion and solving for the Drucker-Prager law with this new coefficient as before. As discussed in section 3.3, we have performed the steady inclined flow protocol with our 0.5 mm beads, which are similar to the one from Jop *et al.* (2005), and extracted the μ_s and μ_2 coefficients from the fit of $\Theta_s(h/d)$ (c.f. figure 6). As expected, we retrieve values close to the ones from Jop *et al.* (2005); for the sake of comparison, and owing to the materials similarities, we have not determined the characteristic inertial number I_0, and have chosen to use the parameters from Jop *et al.* (2005) to perform our $\mu(I)$ simulations: $\mu_s = 0.38$, $\mu_2 = 0.64$ and $I_0 = 0.279$.

Figure 11 shows a comparison of the experimental and computed collapse profiles with the simple Drucker-Prager ($\mu_a = 0.44$) and the $\mu(I)$ ($\mu_s = 0.38$) rheologies. For completeness, we also show the numerical results obtained with a constant μ_s friction coefficient – the lower bound of $\mu(I)$ – in figure 12. For the sake of readability, we focus here on the results for the 15°-inclined configuration; the corresponding comparison figures are provided for all inclinations in figure 20, and support the same observations.

We observe that both the $\mu(I)$ and the constant μ_s rheologies fail to capture accurately the free surface and the static-flowing transition region, in both the dynamical and final resting phases. More precisely, they behave very similarly and both underestimate the flowing threshold, leading to an increased flowability and broader deposits.

The similarity observed between the $\mu(I)$ and constant μ_s rheologies is coherent with the systematic low measured inertial numbers I, as shown in figure 13: except for marginal surface points, the inertial numbers are in the order of at most $I \sim 10^{-2}$ during all the collapse, which is much lower than the characteristic value $I_0 = 0.279$ of the $\mu(I)$ rheology. The additional viscous dissipation introduced by the $\mu(I)$ law compared to a constant μ_s is therefore negligible for such collapses, as was also observed by Valette *et al.* (2019) for horizontal column collapses with a regularised $\mu(I)$ rheology.

The necessary use of a friction coefficient larger than the "stop" friction coefficient μ_s measured from steady inclined plane experiments to quantitatively match experiments was also discussed by Lagrée *et al.* (2011), or Ionescu *et al.* (2015) and Martin *et al.* (2017). The last two explain their increased friction coefficient by the role of the lateral walls, an effect that we shall however discard below (c.f. section 5).

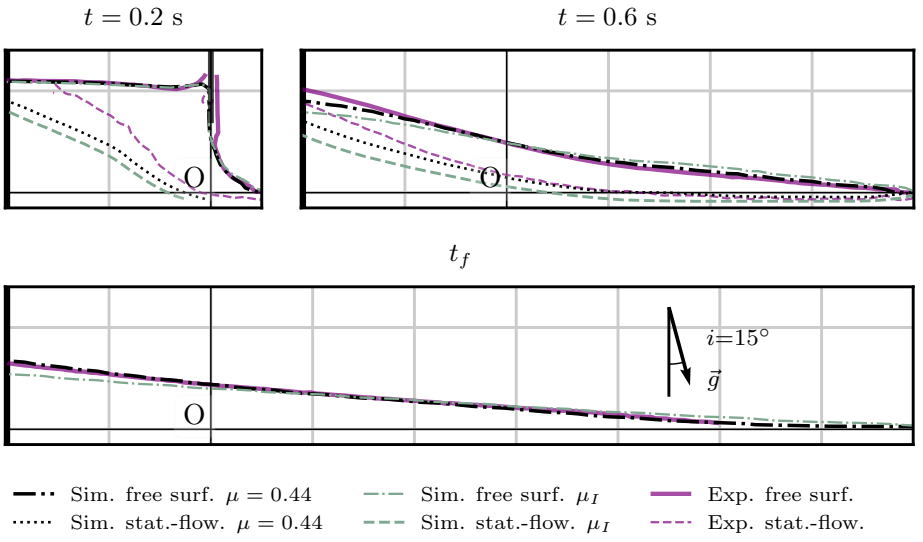

Figure 11: Comparison of 3D simulations performed with $\mu = \mu_a = 0.44$ (black lines) and $\mu = \mu(I)$ (blue lines) for the 15° bead collapse (B15) at $t = 0.2$ s, 0.6 s and t_f. Experimental curves (solid pink line) are provided for reference, and we show both the free-surface lines (resp. plain and dash-dotted) and the static-flowing transition contours (resp. dashed and dotted). The results for the other collapse inclinations can be found in appendix B.1.

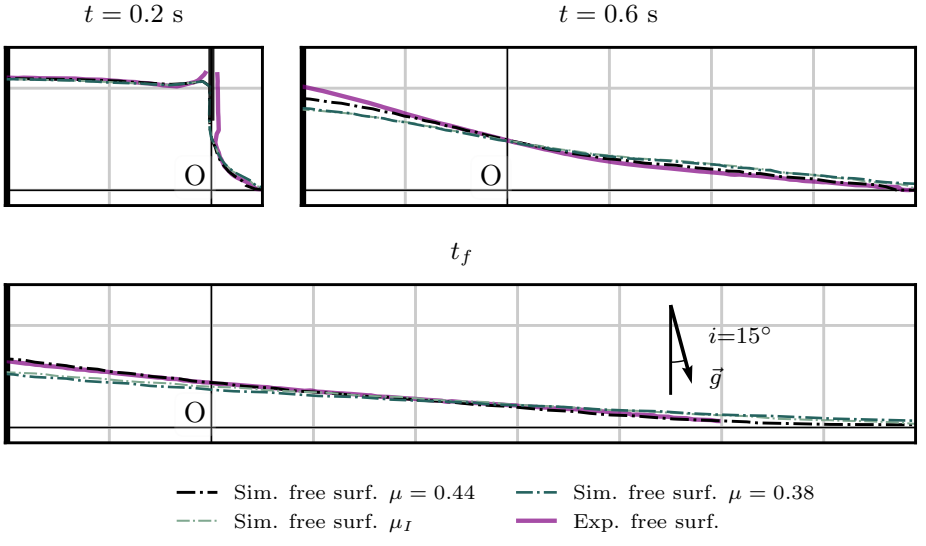

Figure 12: Comparison of 3D simulations performed with $\mu = \mu_a = 0.44$ (black lines), $\mu = \mu(I)$ and $\mu = \mu_s = 0.38$ (blue lines) for the 15° bead collapse (B15) at $t = 0.2$ s, 0.6 s and t_f. Experimental curves (solid pink line) are provided for reference, and we show both the free-surface lines (resp. plain and dash-dotted) and the static-flowing transition contours (resp. dashed and dotted). The results for the other collapse inclinations can be found in appendix B.1.

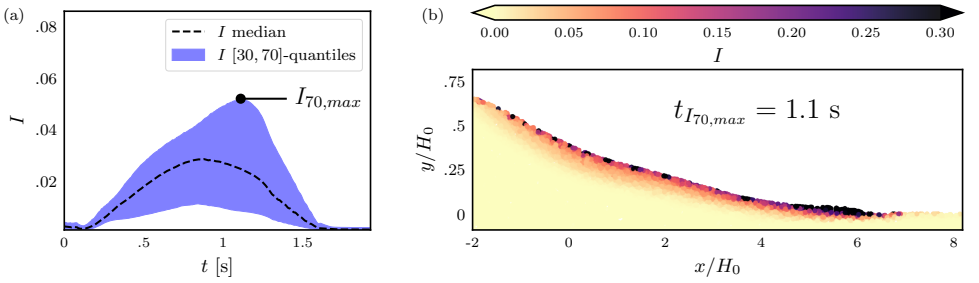

Figure 13: Inertial number I during the simulated 15° bead collapse (B15) with $\mu = \mu_a = 0.44$: (a) Evolution of I as a function of time. Median, 30- and 70-quantiles are estimated in the regions where $I \geqslant 5 \times 10^{-4}$ thereby filtering out static parts of the collapse; (b) Instantaneous inertial number heatmap at $t_{I_{70,max}} = 1.1$ s, i.e. the time for which the 70-quantile of I is maximal. I values remain significantly lower than $I_0 \sim 0.3$ during our collapses explaining why the increase of the friction coefficient from μ_s to μ_2 in the $\mu(I)$ rheology equation (4.2) has a negligible effect. (see movie 5 in the online supplementary material for an animated evolution of the inertial number heatmap)

5. Impact of the sidewalls and scaling laws

Containing walls have been shown to play an important role in the analysis of steady inclined plane experiments, owing to the additional lateral frictional condition they involve, which can strongly affect the free-surface flow velocity (Jop *et al.* 2005). In particular, sidewall friction is responsible for the appearing of super-stable static inclined piles (Taberlet *et al.* 2003) in narrow channels, and substantially affects the apparent rheological parameters for channels of width W below $W/d \lesssim 200$ (Jop *et al.* 2005).

The linear scaling law relating the incline flow thickness to the channel width (Savage 1979; Taberlet *et al.* 2003) has also been used in the context of transient granular collapses by Ionescu *et al.* (2015) to support an increase of the effective 2D friction coefficient, albeit without proper definition of a flow thickness in such configuration.

In the following, we first validate our frictional boundary condition modelling with direct comparison between experimental and simulated collapses using two different channel widths. We also study numerically the impact of the channel width depending on the aspect ratio of the initial column, and favourably compare our results with previously proposed scaling laws. Finally, we use the – consequently validated – simulator to explore the role of wall friction on unsteady non-uniform collapses, by varying the channel width numerically, and determine the corresponding equivalent 2D friction coefficient (which therefore incorporates the friction on the sidewalls).

5.1. *Experimental validation of wall friction effect*

In order to validate our numerical method for the simulation of lateral walls and frictional boundary conditions, we perform dedicated collapse experiments with two different channel widths, and compare the corresponding height profiles with the simulated ones. For simplicity, the granular collapses are performed in a rough horizontal – 0° – channel, with the 0.5 mm glass beads described above. We consider two different channel widths: $W = 1$ cm and $W = 4$ cm, which thus correspond to $W/d = 20$ and 80 respectively. Experimental conditions are similar to the aforementioned 0° collapse, but with initial column dimensions of $H_0 = L_0 = 12$ cm, giving an aspect ratio $a = 1$, which allows us to make the effects of the walls more visible on the final upslope height (c.f. Balmforth & Kerswell (2005) or Zhang *et al.* (2021)), thereby providing a simple measure to compare the effect of lateral friction, which we shall use to determine the corresponding two-dimensional effective friction in

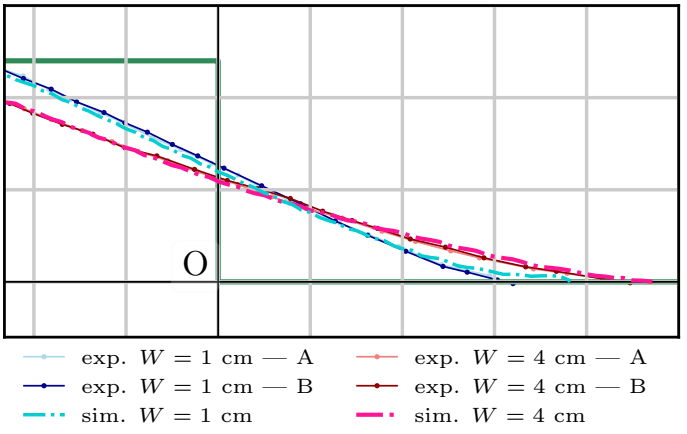

Figure 14: Influence of the sidewalls: rest-state height profiles of simulated and experimental collapses for $a = 1$ and two different widths ($W = 1$ cm and $W = 4$ cm) at 0° slope. Two experimental replicates (A and B) are compared for each width run. The green solid line delineates the initial column with size 0.12×0.12 cm^2. Numerical collapses are performed with a constant internal friction coefficient $\mu = 0.44$ and a friction coefficient between the glass walls and the material $\mu_w = 0.23$.

section 5.3. The corresponding numerical collapses are carried out consistently, using the constant bulk friction coefficient $\mu = 0.44$ and a friction coefficient between the material and the walls $\mu_w = 0.23$.

Figure 14 shows the rest-state height profiles for the simulations and experiments, with two independent experimental runs for each width in order to ensure reliability of the results. We observe that the simulated profiles compare noticeably well with the experimental ones, which underlines the validity of our numerical method, and indicates that a plain Drucker-Prager rheology, with – independently measured – friction coefficients μ and μ_w can accurately account for confinement effects in such transient flows. Note that the good agreement between experiments and simulation observed in the narrow case $W/d = 20$ also suggests that continuum modelling remains valid in this range, at least for such collapse flows.

5.2. *Aspect ratio scaling laws in wide and narrow configurations*

To further explore the validity of our model in the context of varying channel width, we perform simulations in wide and narrow channels using different aspect ratios for the initial granular column, and compare the final run-out and upslope height with previously proposed scaling laws. The normalised rest state run-out L_f and upslope height H_f are shown in figure 15 for 40 simulated collapses in both wide and narrow configurations with aspect ratios $a = H_0/L_0$ varying logarithmically from 1 to 20. The wide configuration is obtained from 3D collapses by setting the wall friction to 0 (which is equivalent to the 2 dimensional collapse situation). The narrow situation corresponds to a 1 cm-wide channel with a wall friction coefficient set to $\mu_w = 0.23$. The granular material considered is again the glass beads, with a bulk friction coefficient of $\mu = 0.44$.

The power-law fits obtained for our data (summarised in table 3) exhibit scaling behaviours similar to the previous experimental and numerical studies from Lajeunesse *et al.* (2004); Balmforth & Kerswell (2005); Lagrée *et al.* (2011); Dunatunga & Kamrin (2015), and in particular feature the already observed change of regime between the short ($a \lesssim 7$), and high ($a > 7$) columns in the *wide* configuration. Note that we also observe the theoretical

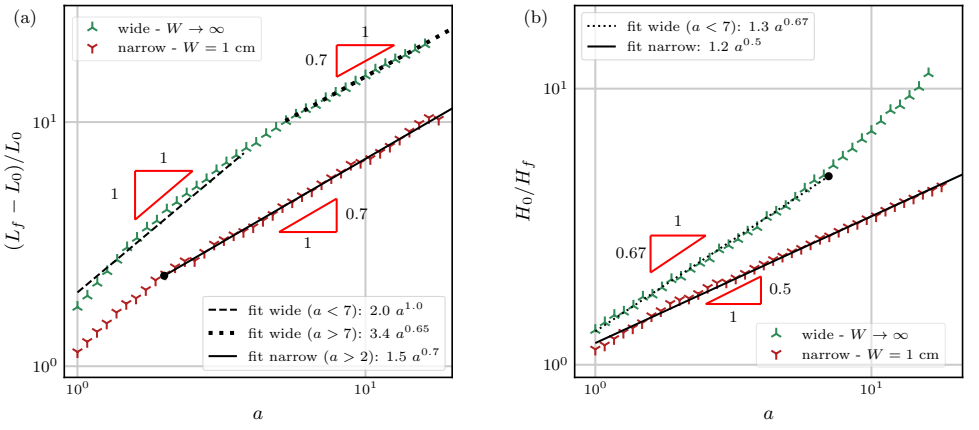

Figure 15: (a) Inverse normalised final upslope height (H_0/H_f) and (b) normalised run-out $(L_f - L_0)/L_0$ as a function of the aspect ratio of the initial column a.

	$\frac{L_f - L_0}{L_0}$	$\frac{H_0}{H_f}$
wide channel	$\begin{cases} 2.0\,a & \text{for } a \lesssim 7 \\ 3.4\,a^{0.65} & \text{for } a \gtrsim 7 \end{cases}$	$1.3\,a^{0.67}$ for $a \lesssim 7$
narrow channel	$1.4\,a^{0.7}$	$1.2\,a^{0.5}$

Table 3: Power-law scaling laws for the run-out and upslope height of the final state of the collapse depending on the initial aspect ratio a.

scaling exponents from the shallow 2D model of Kerswell (2005) and Balmforth & Kerswell (2005), which predicts $H_0/H_f \sim a^{0.69}$ in our aspect ratio range for the *wide* configuration and $H_0/H_f \sim a^{0.5}$ for the narrow one.

Our results also highlight that the scaling behaviour of collapse flows is also well described by the Drucker-Prager rheology with a constant friction coefficient, for aspect ratios up to ~ 10, as long as frictional interaction with the lateral walls is properly accounted for in the narrow case.

5.3. *On the two-dimensional effective friction coefficient*

A linear relation between the flow thickness and the channel width has been reported by Savage (1979); Taberlet *et al.* (2003); Jop *et al.* (2005) in the context of steady inclined granular flows, stating that the presence of friction with the lateral walls can be accounted for by rescaling the friction coefficient as

$$\mu_{eq} = \mu + \mu_w \frac{h}{W} \tag{5.1}$$

where W is the flow width, h the steady flow thickness and μ_w the friction coefficient with the walls. This empirical law, which can be interpreted from force balance principles in the steady flow configuration, has also been used in the context of transient granular collapses by Ionescu *et al.* (2015) to support an increase of the effective 2D friction coefficient, albeit without proper definition of a flow thickness in such framework. In the following, we use our

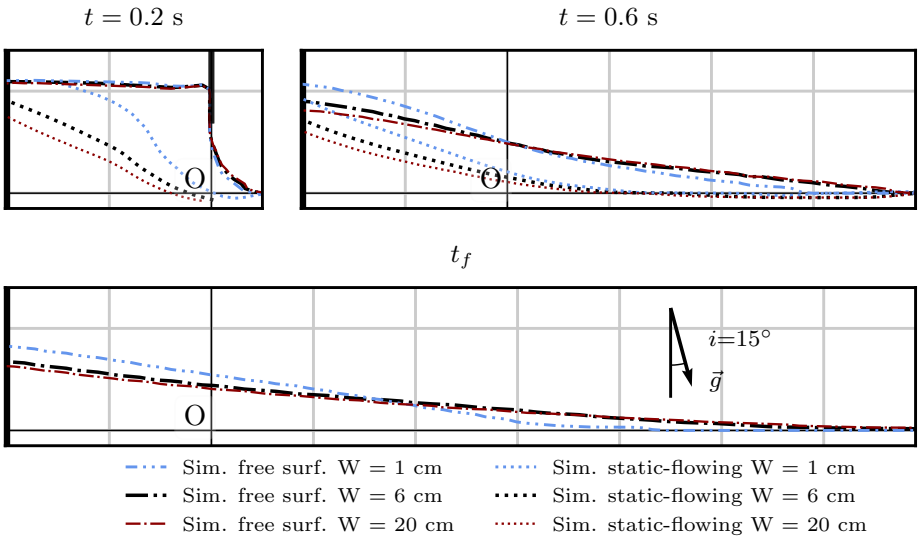

Figure 16: Influence of the sidewalls: comparison of 3D simulations of the 15° bead collapse with several channel widths, and a wall friction coefficient $\mu_w = 0.23$.

validated numerical simulator to explore the relevance of such linear scaling in the context of unsteady flows.

5.3.1. *Impact of the channel width in transient collapses*

To analyse the role of sidewalls friction in the transient collapse context, we first consider the 15°-inclined granular column collapse B15 introduced in section 3.2, and perform several 3D simulations with various channel widths ranging from $W = 1\,\text{cm}$ to $W = 20\,\text{cm}$. The results for transient and final states are shown in figure 16. While the early collapse dynamics, outlined by the static-flowing transition contours, seems impacted for narrow channels, the influence of the width on the free surface height appears negligible for $W > 6\,\text{cm}$, and remains small even for the narrower channel, in particular for the final rest state.

This weak impact of the channel width on the collapse rest state was also observed in the recent Discrete Element Method simulations of Zhang *et al.* (2021), which report negligible impact of the width for $W \gtrsim 20 - 30d$.

5.3.2. *Equivalent 2D friction coefficient*

To further investigate the linear relation (5.1) in the context of unsteady flows, we perform multiple simulations of 3D collapses with many different channel widths, and determine for each 3D simulation (with a given width W) the best equivalent friction coefficient able to reproduce the corresponding 3D collapse with a 2D – unconfined – simulation. Comparison to determine this 2D equivalent coefficient $\mu_{2D,eq}$ is performed on the rest state upslope height H_f, and as such does admittedly not fully allow to replace the 3D simulation by a 2D one, but still provides insight into the role of lateral confinement and friction.

We consider horizontal and 15°-inclined collapses in order to test the robustness of the scaling. As mentioned above, we use an initial column aspect ratio of $a = 1$ to increase the effect of wall friction on H_f. In fact, as already observed by for example Balmforth & Kerswell (2005) or Zhang *et al.* (2021), the upslope part of the column remains static for aspect ratios a below 0.5 in the horizontal case, so that the final upslope height cannot help assess the role of lateral confinement for such stocky collapses.

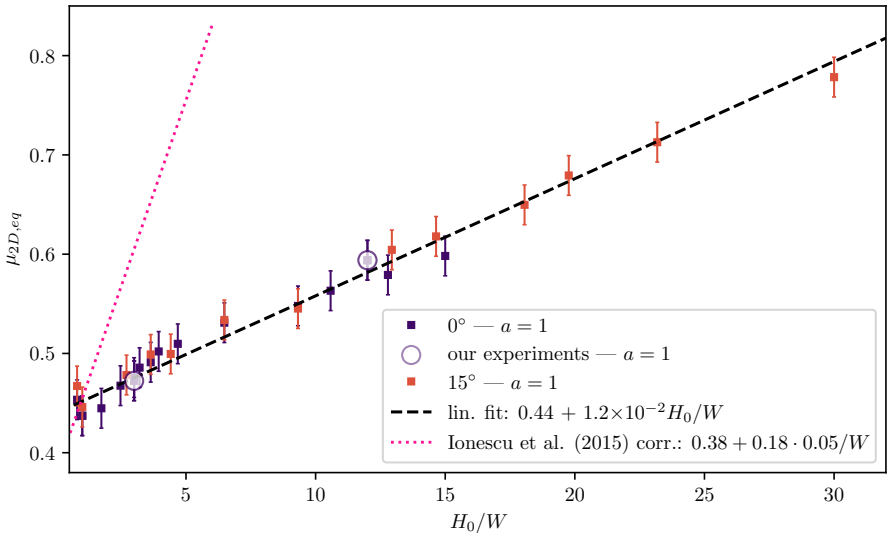

Figure 17: 2D equivalent friction coefficient determined to best match the corresponding 3D final free-surface, as a function of the channel width, for the 0° and 15° beads collapses. Our results seem compatible with a linear dependency, which we illustrate by the dashed fit. We also report the linear scaling (pink dotted line) used by Ionescu *et al.* (2015).

Figure 17 gives the results for channel widths ranging from $W = 20\,\text{cm}$ down to $W = 0.4\,\text{cm}$. Note that we use the initial column height H_0 as a length scale, and consider the non-dimensional width W/H_0, since the flow thickness h is not relevant in our transient case. To compare our data with the linear relation equation (5.1), we plot $\mu_{2D,eq}$ as a function of the inverse non-dimensional width H_0/W.

For the sake of comparison, we also show the linear scaling hypothesis used by Ionescu *et al.* (2015) to obtain the 2D friction coefficient corresponding to the 3D $\mu(I)$ law with an effective flowing thickness estimated at $h \sim 0.05\,\text{m}$ for collapses with $H_0 \sim 0.1\,\text{m}$ (similar to our collapses). This hypothesis was used to account for the confinement effects in narrow collapses within 2D simulations, and typically led to a rescaling of μ_1 from 0.38 to $0.38 + \mu_w 0.05/W \simeq 0.48$ for 10 cm-wide collapses.

We can however observe that our 3D simulations do not support this hypothesis, and exhibit a significantly weaker impact of the lateral walls, as was also suggested in section 5.3.1. Our equivalent 2D friction coefficient nevertheless still appears linearly dependent on H_0/W, with fitted coefficients corresponding to

$$\mu_{2D,eq} = 0.44 + 1.2 \times 10^{-2} \frac{H_0}{W}$$

Interpreted from equation (5.1), it would correspond to an effective flow height $h \simeq 1.2 \times 10^{-2} H_0/\mu_w \simeq 6.3\,\text{mm}$. This value, which is about one order of magnitude lower than the "apparent" collapse flow thickness used by Ionescu *et al.* (2015), is only provided to illustrate that the characteristic length scales involved in steady flows do not directly transpose to the transient case, and that special care is required to properly define the relevant instantaneous quantities.

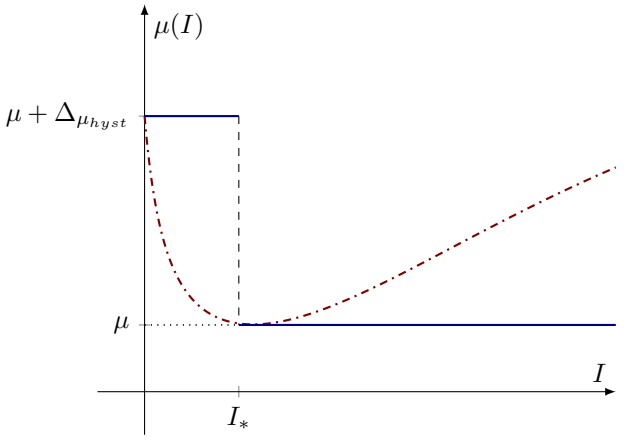

Figure 18: Friction law as a function of the inertial number I. The dash-dotted red curve represents a non-monotonic friction law as expected for granular material (DeGiuli *et al.* 2016). The blue solid line is the simplified law implemented with an hysteresis gap $\Delta\mu_{hyst}$.

6. Transient collapse dynamics and hysteresis phenomenology

Our nonsmooth granular model can accurately predict the material profiles of granular collapses using a single friction coefficient inferred from measured avalanche angles. While generally consistent with experimental measures, the flow dynamics however exhibits significant differences in the early stages of the collapse, as illustrated by the static-flowing transition contours in figure 8 or figure 10. This early deviation, also observed using the $\mu(I)$ rheology by Martin *et al.* (2017), suggests that more complex rheological effects are at play during the onset of the flow, which naturally involves low velocity and hysteresis phenomenology (Pouliquen & Forterre 2002).

As a first step to highlight the role of a static friction coefficient and a potential hysteresis between the solid and flowing phases, we implement a non-constant discontinuous friction coefficient law, somehow reminiscent of the well-known static-dynamic transition in solid friction, using a step function with respect to the inertial number I:

$$\mu_{hyst}(I) = \begin{cases} \mu + \Delta\mu_{hyst} & \text{if } I < I_* \\ \mu & \text{if } I \geqslant I_*, \end{cases} \tag{6.1}$$

as illustrated in figure 18.

The "static" ($I = 0$) friction coefficient is then $\mu+\Delta\mu_{hyst}$, and I^* characterises the transition from "static" to "dynamic" friction. While simpler than the non-monotonic law discussed by DeGiuli & Wyart (2017), our two-valued law still allows for hysteretic instability due to the – in our case discontinuous – decrease of the friction coefficient as I increases, and is chosen in this context to illustrate the potential effects of such phenomenology on transient collapses, paving the way to more elaborate analyses. Note that the increase of the effective friction coefficient at larger I due to collisional dissipation, as predicted by the $\mu(I)$ rheology and used in DeGiuli & Wyart (2017) is also not accounted for in equation (6.1) as we consider only low inertial flows.

Figure 19 shows the results for the 15°-inclined collapse, using the hysteretic law (6.1) with several $\Delta\mu_{hyst}$ and a transition inertial number $I^* = 5 \times 10^{-3}$, consistent with the study

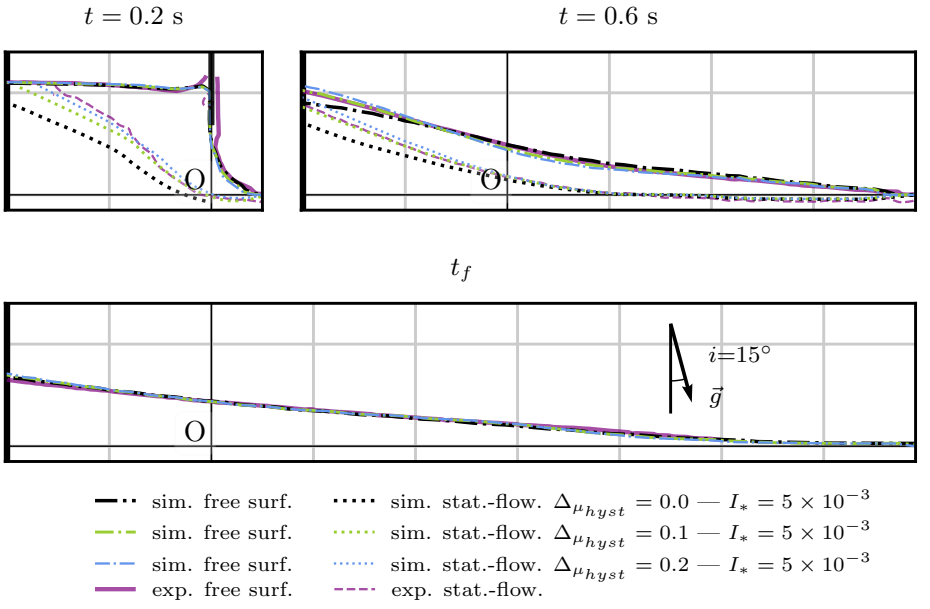

Figure 19: Hysteresis effect on the 15°-collapse (B15): simulation results obtained with the hysteretic law equation (6.1) against experimental profiles and static-flowing transition contours. The simulations are shown for $\Delta\mu_{hyst} = 0$ (no hysteresis), 0.1 and 0.2, and with $\mu = \mu_a = 0.44$ and $I_* = 5 \times 10^{-3}$. See movie 6 in the online supplementary material for a visualisation of the good match in time.

of DeGiuli & Wyart (2017). Despite the simplicity of the law, we observe that the increase of the friction coefficient for very low inertial numbers, described by the $\Delta_{\mu,hyst} \simeq 0.1 - 0.2$ profiles, definitely improves the prediction of the flow dynamics at early stages, and does not affect the final rest state, as expected from such law.

We should stress that the corresponding increase of the "static" friction coefficient (up to $\mu + \Delta\mu_{hyst} = 0.44+0.2 = 0.64$) provided here is only phenomenological, and does not correspond to an independent experimental measurement. However, it suggests that the actual rest-to-flow yield transition, characterised by $\mu(I = 0)$, does not directly correspond to the avalanche friction coefficient, which measurement is highly sensitive to the mechanical noise and could thus incorporate local fluidisation effects (DeGiuli & Wyart 2017). Furthermore, setting a higher $\mu(I = 0)$ than μ_a seems to be consistent with the higher friction coefficient values deduced from tri-axial compression tests on similar micro-metric glass bead materials (Ancey 2001; Adjemian & Evesque 2004; Cui *et al.* 2017) where friction coefficient values range from $\tan 26.5° \sim 0.5$ to $\tan 30° \sim 0.58$, much higher than $\mu_a = 0.44$. The tri-axial configuration allows to measure the yield transition with high pressures, thereby possibly truly approaching the $I \to 0$ limit.

7. Conclusion

Our two- and three-dimensional nonsmooth numerical model can faithfully simulate granular collapses, and quantitatively predict the final deposits for a wide range of bed inclinations, channel widths and column aspect ratios using a fully plastic model with a plain Drucker-Prager rheology. In contrast with previous numerical investigations advocating more complex rheologies (Lagrée *et al.* 2011; Mast *et al.* 2015; Dunatunga & Kamrin 2015), this suggests

that transient granular flows are mostly driven by transitions from flow to rest, and that the final stable states can accurately be described by a unique constant bulk friction coefficient.

Comparisons with experimental collapses furthermore support the use of a friction coefficient corresponding to the avalanche angle, as opposed to the stop angle measured from steady experiments. This observation is not restricted to our numerical study, and was for example also noted by Ionescu *et al.* (2015), albeit not interpreted in this way: while the correction initially attributed to the role of the lateral walls cannot hold in the light of the study provided in section 5, the effective friction coefficient they use turns out to coincide with the avalanche angle measured on their experiment.

Owing to the low inertial numbers involved in the friction-dominated collapse flows, the $\mu(I)$ rheology, which accounts for additional viscous collisional dissipation, is not able to quantitatively improve flow predictions. Furthermore, adjustment of the parameters of the $\mu(I)$ law using steady inclined flow experiments, in particular the *stop* friction coefficient μ_s, appears unable to accurately predict experimental collapse profiles, and systematically underestimates frictional dissipation within the material.

Studying the effect of friction on the lateral walls on three-dimensional simulated collapses in narrow flumes with various widths, we showed that a linear rescaling of the bulk friction coefficient for predicting two-dimensional collapses is still valid but with an effective granular flow depth much smaller than the initial column height. Thus, performing collapses in flumes with widths on the order of the column height results in negligible impact of the wall friction.

As a first step to explore low-velocity extensions of the rheology, we have implemented a simple hysteretic law inspired by the work of Pouliquen & Forterre (2002) and DeGiuli & Wyart (2017). This two-valued rheology, reminiscent of the static and dynamic regimes of Coulomb friction, significantly improves the prediction of the collapse dynamics, especially at the onset of the flow.

Our non-smooth solver provide good predictions of complex 3D granular flows involving high granular deformations and interactions with frictional surfaces. However, the full potential of Sand6 supporting cohesion and dynamic interaction with complex objects remains to be fully exploited. A next step would be to simulate full 3D steady flows with well controlled frictional boundary conditions and compare them to experiments in order to accurately bridge the gap between the constant friction rheology and the $\mu(I)$ rheology.

Supplementary data. In this preprint version movies are available at
https://drive.switch.ch/index.php/s/xnxlGVw40Eh0KUt

Acknowledgements. We would like to thank Olivier Pouliquen, Pierre-Yves Lagrée, Ioan Ionescu, Hugo Perrin, and Matthieu Wyart for their insights during this research study. We are grateful to Christophe Ancey, who graciously let us make experiments in the Environmental Hydraulic Laboratory at EPFL (Switzerland).

Funding. This research was supported by EPFL, Inria, the ERC grant GEM (StG-2014-639139), and TU Wien.

Declaration of interests. The authors report no conflict of interest.

Data availability statement. Data and Python scripts used for plotting figures are archived at Zenodo
https://doi.org/10.5281/zenodo.7288829

Author contributions. G. R. and H. R. conducted the granular experiments. G. D., G. R. and T. M. adapted the Sand6 software to perform numerical collapses. G. R. and T. M. conducted the numerical experiments. G. R., T. M. and F. B.-D. analysed the comparisons results and performed the main scientific investigations. G. R., T. M. and F. B.-D. wrote the paper. All authors proofread the paper.

Appendix A. Numerical method

A.1. *Modified Fischer-Burmeister function for the Drucker-Prager rheology*

In this appendix, we give some details regarding the modified second-order cone Fischer-Burmeister complementarity function f_{MFB} mentioned in section 2.3 to impose the non-smooth Drucker-Prager rheology (2.7). Note that, while we use the SAND6 implementation from (Daviet & Bertails-Descoubes 2016*b*) for our simulations, the presentation given here differs from the original one ((Daviet & Bertails-Descoubes 2016*b*,*a*; Daviet *et al.* 2011)) and avoids the need to introduce parallels between Coulomb friction and the Drucker-Prager rheology.

The first step to reformulate the Drucker-Prager rheology (2.7) as a root-finding problem is to recast it as second-order cone complementarity problem (SOCCP). We introduce the second-order cone

$$\mathcal{K}_\mu = \left\{ \boldsymbol{\tau} \in S(d);\ \|\text{Dev}\,(\boldsymbol{\tau})\| \leqslant \mu \frac{\text{Tr}\,(\boldsymbol{\tau})}{\sqrt{2d}} \right\} \tag{A 1}$$

where $S(d)$ denotes the space of $d \times d$ symmetric rank-2 tensors, with dimension $s_d = \frac{d(d+1)}{2}$, which can be decomposed as an orthogonal sum between the space generated by the unit basis vector $\boldsymbol{\iota}_d \equiv \sqrt{\frac{2}{d}}\mathbb{I}_d$ and the space of traceless symmetric tensors: $S(d) = \text{Span}\,\{\boldsymbol{\iota}_d\} \oplus T(d)$.

As shown in (Daviet & Bertails-Descoubes 2016*a*), the Drucker-Prager rheology (2.7) is equivalent to the SOCCP

$$(\boldsymbol{\gamma}, \boldsymbol{\lambda}) \in \mathcal{DP}(\mu) \iff \mathcal{K}_{\tilde{\mu}} \ni \boldsymbol{\lambda} \perp \tilde{\boldsymbol{\gamma}} \in \mathcal{K}_{\frac{1}{\tilde{\mu}}} \tag{A 2}$$

with

$$\tilde{\mu} = \sqrt{\frac{2}{d}}\,\mu \tag{A 3}$$

and

$$\begin{aligned} \tilde{\boldsymbol{\gamma}} &= \boldsymbol{\gamma} + \tilde{\mu}\,\|\text{Dev}\,(\boldsymbol{\gamma})\|\,\boldsymbol{\iota}_d \\ &= \boldsymbol{\gamma} + \tilde{\mu}\sqrt{\frac{2}{d}}\,\|\text{Dev}\,(\boldsymbol{\gamma})\|\,\mathbb{I}_d. \end{aligned} \tag{A 4}$$

Note that the SOCCP is expressed in terms of $\tilde{\mu}$ instead of μ to exhibit symmetry in the SOCCP inclusions in $\mathcal{K}_{\tilde{\mu}}$ and its dual cone $\mathcal{K}_{\frac{1}{\tilde{\mu}}}$.

Equation (A 2) can be further symmetrised and put in a canonical self-dual form with the additional change of variable

$$\begin{aligned} \hat{\boldsymbol{\lambda}} &= \tilde{\mu}\,\frac{\text{Tr}\,(\boldsymbol{\lambda})}{\sqrt{2d}}\,\boldsymbol{\iota}_d + \text{Dev}\,(\boldsymbol{\lambda}) \\ &= \tilde{\mu}\,\frac{\text{Tr}\,(\boldsymbol{\lambda})}{d}\,\mathbb{I}_d + \text{Dev}\,(\boldsymbol{\lambda}) \\ \hat{\tilde{\boldsymbol{\gamma}}} &= \frac{\text{Tr}\,(\tilde{\boldsymbol{\gamma}})}{\sqrt{2d}}\,\boldsymbol{\iota}_d + \tilde{\mu}\,\text{Dev}\,(\tilde{\boldsymbol{\gamma}}) \\ &= \frac{\text{Tr}\,(\tilde{\boldsymbol{\gamma}})}{d}\,\mathbb{I}_d + \tilde{\mu}\,\text{Dev}\,(\tilde{\boldsymbol{\gamma}}) \end{aligned} \tag{A 5}$$

so that

$$(\boldsymbol{\gamma}, \boldsymbol{\lambda}) \in \mathcal{DP}(\mu) \iff \mathcal{K}_1 \ni \hat{\boldsymbol{\lambda}} \perp \hat{\tilde{\boldsymbol{\gamma}}} \in \mathcal{K}_1. \tag{A 6}$$

where $\mathcal{K}_1 = \left\{ \boldsymbol{\tau} \in S(d);\ \|\text{Dev}\,(\boldsymbol{\tau})\| \leqslant \frac{\text{Tr}(\boldsymbol{\tau})}{\sqrt{2d}} \right\}$ can also be identified as the self-

dual Lorentz cone in $\mathbb{R}^{s_d-1}$ using the natural orthonormal isomorphism between $(S(d) = \mathrm{Span}\{\iota_d\} \oplus T(d), \langle\bullet,\bullet\rangle)$ and $\left(\mathbb{R}\oplus\mathbb{R}^{s_d-1}, \bullet\cdot\bullet\right)$.

The new symmetric SOCCP (A 6) now falls directly in the framework of Fukushima *et al.* (2002), which allows to rewrite it as a root-finding problem on a *modified* Fischer-Burmeister function

$$(\boldsymbol{\gamma},\boldsymbol{\lambda}) \in \mathcal{DP}(\mu) \iff f_{\mathrm{MFB}}(\boldsymbol{\gamma},\boldsymbol{\lambda}) = 0. \tag{A 7}$$

with

$$\begin{aligned} f_{\mathrm{MFB}} : S(d)\times S(d) &\to S(d) \\ (\boldsymbol{\gamma},\boldsymbol{\lambda}) &\mapsto f_{\mathrm{FB}}(\hat{\boldsymbol{\gamma}},\hat{\boldsymbol{\lambda}}) \end{aligned} \tag{A 8}$$

where

$$f_{\mathrm{FB}}(\hat{\boldsymbol{\gamma}},\hat{\boldsymbol{\lambda}}) = \left(\mathrm{Tr}\left(\hat{\boldsymbol{\gamma}}\right) + \mathrm{Tr}\left(\hat{\boldsymbol{\lambda}}\right) - s\right)\frac{\mathbb{I}_d}{d} + \left(1 - \frac{\mathrm{Tr}\left(\hat{\boldsymbol{\gamma}}\right)}{s}\right)\mathrm{Dev}\left(\hat{\boldsymbol{\gamma}}\right) + \left(1 - \frac{\mathrm{Tr}\left(\hat{\boldsymbol{\lambda}}\right)}{s}\right)\mathrm{Dev}\left(\hat{\boldsymbol{\lambda}}\right)$$

$$s = \sqrt{d\left(\|\hat{\boldsymbol{\gamma}}\|^2 + \|\hat{\boldsymbol{\lambda}}\|^2 + \sqrt{\left(\|\hat{\boldsymbol{\gamma}}\|^2 + \|\hat{\boldsymbol{\lambda}}\|^2\right)^2 - \frac{2}{d}\left\|\mathrm{Tr}\left(\hat{\boldsymbol{\gamma}}\right)\mathrm{Dev}\left(\hat{\boldsymbol{\gamma}}\right) + \mathrm{Tr}\left(\hat{\boldsymbol{\lambda}}\right)\mathrm{Dev}\left(\hat{\boldsymbol{\lambda}}\right)\right\|^2}\right)}. \tag{A 9}$$

A.2. *Spatial discretization*

We discretise the conservations equations (2.2 – 2.3) using the material point method (MPM) (Sulsky *et al.* 1995; Bardenhagen *et al.* 2000), which leverages both an Eulerian grid to enforce momentum conservation and a Lagrangian particle representation to resolve transport terms.

The volume fraction field ϕ is thus approximated as a set of N material points $(\boldsymbol{x}_p)_{1\leqslant p\leqslant N}$ with finite material volume V_p and velocity $\boldsymbol{v}_p$, following the mathematical distribution

$$\phi(\boldsymbol{x},t) = \sum_p V_p\,\delta\left(\boldsymbol{x} - \boldsymbol{x}_p(t)\right). \tag{A 10}$$

Discrete-time mass conservation (2.6) is then achieved by advecting the particles over each time-step in a semi-implicit way as $\boldsymbol{x}_p^{(n+1)} = \boldsymbol{x}_p^{(n)} + \delta t\,\boldsymbol{v}_p^{(n+1)}$, with $\boldsymbol{v}_p^{(n+1)}$ sampled from the continuous velocity field $\boldsymbol{u}$ as $\boldsymbol{v}_p^{(n+1)} = \boldsymbol{u}^{(n+1)}\left(\boldsymbol{x}_p^{(n)}\right)$.

The material derivative $\frac{D\boldsymbol{u}}{Dt}$ in the momentum conservation equation (2.2) is first discretised in time as $\frac{\boldsymbol{u}^{(n+1)}-\boldsymbol{u}^{(*)}}{\delta t}$, where $\boldsymbol{u}^{(*)}$ is the velocity field recovered by transferring back the particle velocity from the previous time-step to the grid. In practice, we use the APIC velocity transfer scheme from Jiang *et al.* (2015).

In order to discretise the momentum conservation equation in space, we first rewrite the Cauchy stress without loss of generality as $\boldsymbol{\sigma} = \phi\hat{\boldsymbol{\sigma}}$, and similarly, $\boldsymbol{\lambda} = \phi\hat{\boldsymbol{\lambda}}$ and $\boldsymbol{f} = \phi\hat{\boldsymbol{f}}$. We recall that the Drucker–Prager rheology is invariant with respect to a positive scaling factor on the stress (Daviet & Bertails-Descoubes 2016*b*), so that $(\boldsymbol{\gamma},\boldsymbol{\lambda}) \in \mathcal{DP}(\mu) \iff (\boldsymbol{\gamma},\hat{\boldsymbol{\lambda}}) \in \mathcal{DP}(\mu)$.

Now, let $V \subset H_0^1(\Omega)$ be a discrete space of square-integrable velocity fields with square-integrable gradients over Ω, and $T \subset L^2(\Omega)$ a space of square-integrable symmetric tensor fields. Note that in practice, we use the space of trilinear shape functions over a regular

Cartesian grid for both U and T. Equation (2.3) corresponds to the variational formulation

$$\rho_g \int_\Omega \phi \boldsymbol{w}^T \frac{\boldsymbol{u}^{(n+1)} - \boldsymbol{u}^*}{\delta t} - \int_\Omega \boldsymbol{w}^T \nabla \cdot \left[\phi \hat{\boldsymbol{\lambda}}\right] = \int_\Omega \phi \boldsymbol{w}^T \hat{\boldsymbol{f}}, \quad \forall \boldsymbol{w} \in V,$$

or after integration by parts,

$$\rho_g \int_\Omega \phi \boldsymbol{w}^T \frac{\boldsymbol{u}^{(n+1)} - \boldsymbol{u}^*}{\delta t} + \int_\Omega \nabla \boldsymbol{w} : \left[\phi \hat{\boldsymbol{\lambda}}\right] = \int_\Omega \phi \boldsymbol{w}^T \hat{\boldsymbol{f}} - \int_{\partial\Omega} \phi \boldsymbol{w}^T \hat{\boldsymbol{\lambda}} \boldsymbol{n}, \quad \forall \boldsymbol{w} \in V. \tag{A 11}$$

Note that the boundary term vanishes if either Dirichlet boundary conditions are used or the domain extends sufficiently far away from the material such that $\phi_{|\partial\Omega} = 0$.

Using the discrete expression for ϕ (A 10), we can rewrite the variational mass conservation (A 11) as

$$a(\boldsymbol{u}, \boldsymbol{w}) = b(\boldsymbol{u}, \boldsymbol{w}) + l(\boldsymbol{w}) \quad \forall \boldsymbol{w} \in V \tag{A 12}$$

with

$$\begin{aligned} a(\boldsymbol{u}, \boldsymbol{w}) &:= \frac{\rho_g}{\delta t} \sum_p V_p \boldsymbol{w}(\boldsymbol{x}_p)^T \boldsymbol{u}(\boldsymbol{x}_p) \\ b(\hat{\boldsymbol{\lambda}}, \boldsymbol{w}) &:= \sum_p V_p (\nabla w)(\boldsymbol{x}_p) : \hat{\boldsymbol{\lambda}}(\boldsymbol{x}_p) \\ l(\boldsymbol{w}) &:= \sum_p V_p \left[\hat{f} + \boldsymbol{w}(\boldsymbol{x}_p)^T \boldsymbol{u}^{(*)}(\boldsymbol{x}_p)\right]. \end{aligned}$$

Similarly, we write the definition of the auxiliary strain rate tensor $\boldsymbol{\gamma}$ in a variational form as

$$\int_\Omega \boldsymbol{\gamma} : \boldsymbol{\tau} = \int_\Omega \phi \nabla \boldsymbol{u} : \boldsymbol{\tau} + \frac{1}{\delta t} \int_\Omega \left[\phi - \phi^c\right] \frac{1}{d} \mathbb{I} : \boldsymbol{\tau} \quad \forall \boldsymbol{\tau} \in T,$$

or equivalently

$$s(\boldsymbol{\gamma}, \boldsymbol{\tau}) = b(\boldsymbol{\tau}, \boldsymbol{w}) + k(\boldsymbol{\tau}) \quad \forall \boldsymbol{\tau} \in T \tag{A 13}$$

with

$$\begin{aligned} s(\boldsymbol{\gamma}, \boldsymbol{\tau}) &:= \int_\Omega \boldsymbol{\gamma} : \boldsymbol{\tau} \\ k(\boldsymbol{\tau}) &:= \frac{1}{d\delta t} \sum_p V_p \mathbb{I} : \boldsymbol{\tau} - \frac{1}{d\delta t} \int_\Omega \phi^c \mathbb{I} : \boldsymbol{\tau} \end{aligned}$$

The discrete system is then obtained by assembling the matrices M, B, S and vectors $\boldsymbol{l}, \boldsymbol{k}$ corresponding to the bilinear forms m, b, s and linear forms a, b, s and linear forms l, k, respectively. Note however that we follow the suggestions from (Daviet & Bertails-Descoubes 2016*b*,*a*) to replace the matrix M with its lumped diagonal version $\hat{M}$ defined as that $\hat{M}_{i,j} = \delta_i^j \sum_k M_{i,k}$ (which is consistent with our use of the APIC particle–grid transfer scheme) and to replace S with the identity matrix (which amounts to perform numerical integration of s using the trapezoidal rule).

This finally leads to the algebraic problem

$$\text{Find } \boldsymbol{u}, \boldsymbol{\gamma}, \hat{\boldsymbol{\lambda}} \in R^d \times S(d) \times S(d) \text{ s.t.} \\ \begin{cases} \hat{M}\boldsymbol{u} = B^T \hat{\boldsymbol{\lambda}} + \boldsymbol{l} \\ \boldsymbol{\gamma} = B\boldsymbol{u} + \boldsymbol{k} \\ (\boldsymbol{\gamma}, \boldsymbol{\lambda}) \in \mathcal{DP}(\mu), \end{cases} \tag{A 14}$$

from which we can eliminate the velocity variable $\boldsymbol{u}$ by introducting the Schur complement $W := B\hat{M}^{-1}B^T$, yielding problem (2.9).

Note that the constrained algebraic problem equation (A 14) can naturally be extended to incorporate rigid body dynamics, with two-way frictional boundary interaction with the granular material obeying a Coulomb-like condition. Details regarding the coupling with rigid bodies are provided in Daviet & Bertails-Descoubes (2016*b*).

A.3. *Gauss-Seidel algorithm*

Problem (2.9) could be solved with any technique able to address discrete Coulomb friction problems; here we follow the method of Daviet *et al.* (2011), which is itself a variant of the Non-Smooth Contact Dynamics (Jean 1999) algorithm.

In this approach, the contacts (here, the instances of the Drucker–Prager condition 2.7) are repeatedly solved one by one in a Gauss-Seidel approach: at the k^{th} iteration of the algorithm, and for each discrete degree of freedom i of our tensor fields, we solve for the local stress $\boldsymbol{\lambda}_i^{[k+1]}$ assuming that all other stress degrees of freedom are frozen, i.e.

$$\text{Find } \boldsymbol{\gamma}_i^{[k+1]}, \boldsymbol{\lambda}_i^{[k+1]} \in S(d) \times S(d) \text{ s.t.} \\ \begin{cases} \boldsymbol{\gamma}_i^{[k+1]} = \boldsymbol{W_{ii}} \boldsymbol{\lambda_i}^{[k+1]} + \underbrace{\boldsymbol{b}_i + \sum_{j<i} \boldsymbol{W_{ij}} \boldsymbol{\lambda_j}^{[k+1]} + \sum_{i>j} \boldsymbol{W_{ij}} \boldsymbol{\lambda_j}^{[k]}}_{\boldsymbol{b}_i^{[k+1]}} \\ (\boldsymbol{\gamma}_i^{[k+1]}, \boldsymbol{\lambda}_i^{[k+1]}) \in \mathcal{DP}(\mu). \end{cases} \tag{A 15}$$

iterating (on k) until convergence.

The local problem A 15 is equivalent to solving

$$f_{\text{MFB}}(\boldsymbol{W_{ii}} \boldsymbol{\lambda_i}^{[k+1]} + \boldsymbol{b}_i^{[k+1]}, \boldsymbol{\lambda_i}^{[k+1]}) = 0,$$

which we do using a generalised (non-smooth) Newton algorithm.

Note that for $d = 2$, the dimension of S_d is 3, which means the problem has a structure similar to that of discrete Coulomb friction. In this case, we directly reuse the solver from (Daviet *et al.* 2011), which combines the Newton-based optimization problem with an analytical solver based on finding the roots of a degree-4 polynomial. For $d = 3$, the dimension of S_d is 6, and to the best of our knowledge, no analytical solver is available. We thus use the Newton-based solver only.

Appendix B. Additional results

B.1. *Comparison of the different rheologies*

Figure 20 collects the exhaustive comparisons between the $\mu = \mu_a$, the $\mu = \mu_s$ and $\mu = \mu(I)$ rheologies on bead collapses for all inclinations.

It supports the observations of section 4.4, highlighting the systematic underestimation of the internal friction by the μ_s and $\mu(I)$ rheologies, which give very similar results.

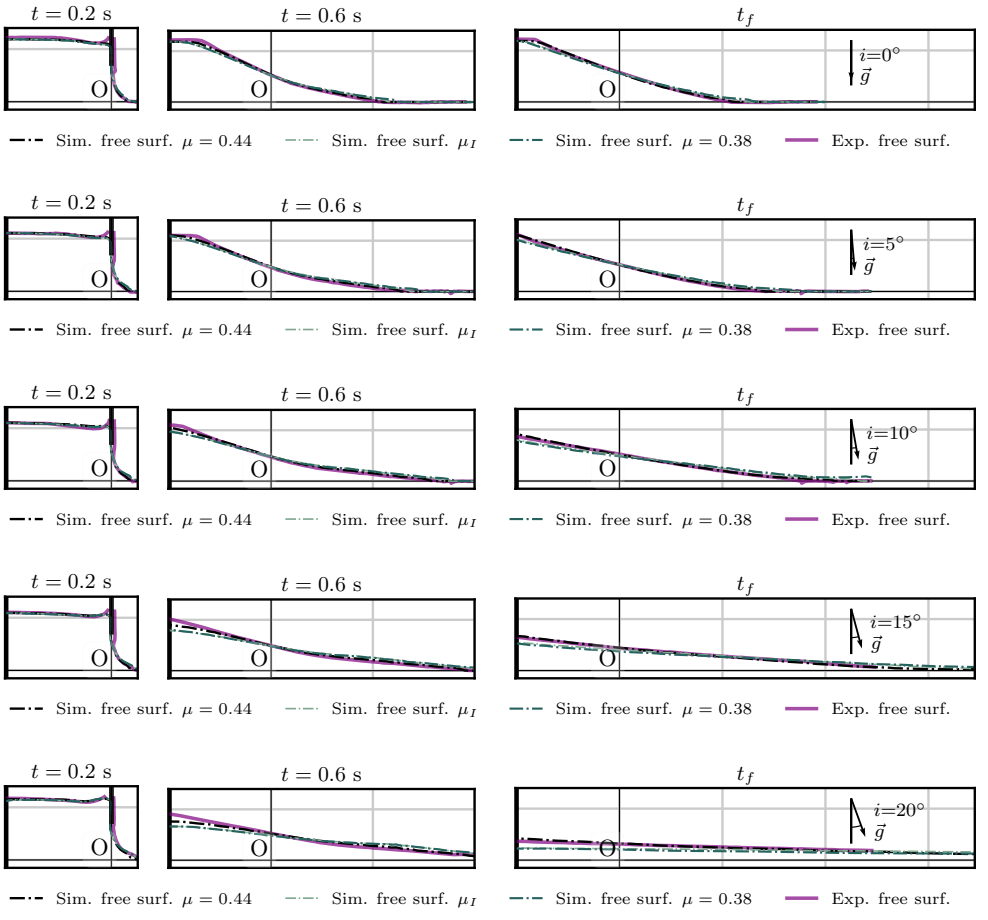

Figure 20: Comparison of 3D simulations performed with $\mu = \mu_a = 0.44$ (black lines), $\mu = \mu(I)$ and $\mu = \mu_s = 0.38$ (blue lines) for the all the bead collapses at $t = 0.2$ s, 0.6 s and t_f. Experimental curves (solid pink line) are provided for reference, and we show both the free-surface lines (resp. plain and dash-dotted) and the static-flowing transition contours (resp. dashed and dotted).

B.2. *Impact of the lifting gate*

In order to check the weak impact of friction between the granular material and the lifting gate, we have run a simulation with a non-realistically high granular-gate friction coefficient $\mu_D = 1$, and compared with the value used in the paper ($\mu_D = 0.18$). Both simulations use the same bulk coefficient corresponding to the bead material ($\mu = 0.44$) and the same numerical parameters. The resulting height profiles and static-flowing transition contours in figure 21 show that while friction with the gate can indeed affect very locally the profile close to the door for early times, it does not impact the flow once the gate is fully lifted, and gives the same collapse free-surface and overall dynamics.

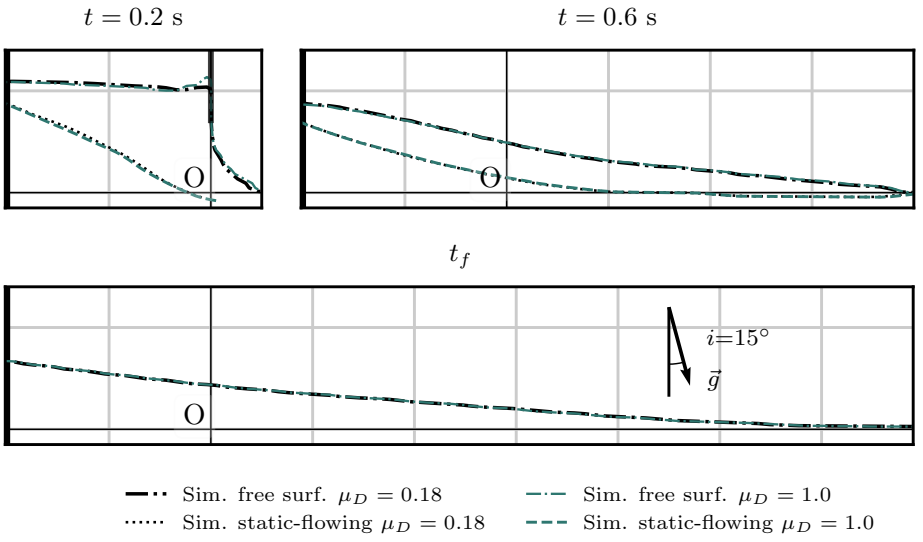

Figure 21: Impact of the lifting gate friction: comparison of simulations of the 15° bead collapse with the standard friction coefficient between the material and the door $\mu_D = 0.18$ (black lines) and a non-realistic high coefficient $\mu_D = 1$ (green lines).

REFERENCES

Adjemian, F. & Evesque, P. 2004 Experimental study of stick-slip behaviour. *Int. J. Numer. Analyt. Meth. Geomech.* **28** (6), 501–530.

Ancey, C. 2001 Dry granular flows down an inclined channel: Experimental investigations on the frictional-collisional regime. *Phys. Rev. E* **65** (1), 011304.

Andreotti, B., Forterre, Y. & Pouliquen, O. 2013 *Granular media: between fluid and solid*. Cambridge University Press.

Artoni, R., Santomaso, A. & Canu, P. 2011 Hysteresis in a hydrodynamic model of dense granular flows. *Phys. Rev. E* **83** (5), 051304.

Azéma, E. & Radjai, F. 2014 Internal structure of inertial granular flows. *Phys. Rev. Lett.* **112** (7), 078001.

Balmforth, N.J. & Kerswell, R.R. 2005 Granular collapse in two dimensions. *J. Fluid Mech.* **538**, 399–428.

Bardenhagen, S.G., Brackbill, J.U. & Sulsky, D. 2000 The material-point method for granular materials. *Comput. Methods Appl. Mech. Eng.* **187** (3-4), 529–541.

Chupin, L., Dubois, T., Phan, M. & Roche, O. 2021 Pressure-dependent threshold in a granular flow: Numerical modeling and experimental validation. *J. Non-Newtonian Fluid Mech.* **291**, 104529.

Cui, D., Wu, W., Xiang, W., Doanh, T., Chen, Q., Wang, S., Liu, Q. & Wang, J. 2017 Stick-slip behaviours of dry glass beads in triaxial compression. *Granul. Matter* **19** (1), 1–18.

Da Cruz, F, Chevoir, F, Bonn, Daniel & Coussot, Ph 2002 Viscosity bifurcation in granular materials, foams, and emulsions. *Phys. Rev. E* **66** (5), 051305.

Da Cruz, F., Emam, S., Prochnow, M., Roux, J.-N. & Chevoir, F. 2005 Rheophysics of dense granular materials: Discrete simulation of plane shear flows. *Phys. Rev. E* **72** (2), 021309.

Daerr, A. & Douady, S. 1999 Two types of avalanche behaviour in granular media. *Nature* **399** (6733), 241–243.

Daviet, G. & Bertails-Descoubes, F. 2016*a* Nonsmooth simulation of dense granular flows with pressure-dependent yield stress. *J. Non-Newtonian Fluid Mech.* **234**, 15–35.

Daviet, G. & Bertails-Descoubes, F. 2016*b* A semi-implicit material point method for the continuum simulation of granular materials. *ACM Trans. Graph.* **35** (4), 102.

Daviet, G., Bertails-Descoubes, F. & Boissieux, L. 2011 A hybrid iterative solver for robustly capturing coulomb friction in hair dynamics. In *Proceedings of the 2011 SIGGRAPH Asia Conference*, pp. 1–12.

DeGiuli, E., McElwaine, J. N. & Wyart, M. 2016 Phase diagram for inertial granular flows. *Phys. Rev. E* **94** (1), 012904.

DeGiuli, E. & Wyart, M. 2017 Friction law and hysteresis in granular materials. *Proc. Natl. Acad. Sci. U.S.A.* **114** (35), 9284–9289.

Drucker, D. C. & Prager, W. 1952 Soil mechanics and plastic analysis or limit design. *Quarterly of applied mathematics* **10** (2), 157–165.

Dunatunga, S. & Kamrin, K. 2015 Continuum modelling and simulation of granular flows through their many phases. *J. Fluid Mech.* **779**, 483–513.

Farin, M., Mangeney, A. & Roche, O. 2014 Fundamental changes of granular flow dynamics, deposition, and erosion processes at high slope angles: insights from laboratory experiments. *J. Geophys. Res Earth Surf.* **119** (3), 504–532.

Forterre, Y. & Pouliquen, O. 2003 Long-surface-wave instability in dense granular flows. *J. Fluid Mech.* **486**, 21–50.

Franci, A. & Cremonesi, M. 2019 3d regularized μ (I)-rheology for granular flows simulation. *J. Comput. Phys.* **378**, 257–277.

Fukushima, M., Luo, Z.-Q. & Tseng, P. 2002 Smoothing functions for second-order-cone complementarity problems. *SIAM Journal on optimization* **12** (2), 436–460.

Gaume, J., Gast, T., Teran, J., van Herwijnen, A. & Jiang, C. 2018 Dynamic anticrack propagation in snow. *Nature communications* **9** (1), 3047.

Hutter, K. & Koch, T. 1991 Motion of a granular avalanche in an exponentially curved chute: experiments and theoretical predictions. *Phil. Trans. Roy. Soc. London A* **334** (1633), 93–138.

Ionescu, I.R., Mangeney, A., Bouchut, F. & Roche, O. 2015 Viscoplastic modeling of granular column collapse with pressure-dependent rheology. *J. Non-Newtonian Fluid Mech.* **219**, 1–18.

Jean, M. 1999 The non-smooth contact dynamics method. *Computer Methods in Applied Mechanics and Engineering* **177** (3), 235–257.

Jiang, C., Schroeder, C., Selle, A., Teran, J. & Stomakhin, A. 2015 The affine particle-in-cell method. *ACM Trans. Graph.* **34** (4), 51.

Jop, P., Forterre, Y. & Pouliquen, O. 2005 Crucial role of sidewalls in granular surface flows: consequences for the rheology. *J. Fluid Mech.* **541**, 167–192.

Jop, P., Forterre, Y. & Pouliquen, O. 2006 A constitutive law for dense granular flows. *Nature* **441** (7094), 727–30.

Kerswell, R.R. 2005 Dam break with coulomb friction: A model for granular slumping? *Phys. Fluids* **17** (5), 057101.

Klár, G., Gast, Th., Pradhana, A., Fu, C.and Schroeder, C., Jiang, C. & Teran, J. 2016 Drucker-prager elastoplasticity for sand animation. *ACM Trans. Graph.* **35** (4), 1–12.

Lacaze, L. & Kerswell, R.R. 2009 Axisymmetric granular collapse: a transient 3d flow test of viscoplasticity. *Phys. Rev. Lett.* **102** (10), 108305.

Lacaze, L., Phillips, J.C. & Kerswell, R.R. 2008 Planar collapse of a granular column: Experiments and discrete element simulations. *Phys. Fluids* **20** (6), 063302.

Lagrée, P.-Y., Staron, L. & Popinet, S. 2011 The granular column collapse as a continuum: validity of a two-dimensional navier–stokes model with a μ (I)-rheology. *J. Fluid Mech.* **686**, 378–408.

Lajeunesse, E., Mangeney-Castelnau, A. & Vilotte, J.P. 2004 Spreading of a granular mass on a horizontal plane. *Phys. Fluids* **16** (7), 2371–2381.

Mangeney-Castelnau, A., Bouchut, F., Vilotte, J.P., Lajeunesse, E., Aubertin, A. & Pirulli, M. 2005 On the use of saint venant equations to simulate the spreading of a granular mass. *Journal of Geophysical Research: Solid Earth* **110** (B9).

Martin, N., Ionescu, I.R., Mangeney, A., Bouchut, F. & Farin, M. 2017 Continuum viscoplastic simulation of a granular column collapse on large slopes: μ (I) rheology and lateral wall effects. *Phys. Fluids* **29** (1), 013301.

Mast, C.M., Arduino, P., Mackenzie-Helnwein, P. & Miller, G.R. 2015 Simulating granular column collapse using the material point method. *Acta Geotechnica* **10** (1), 101–116.

MiDi, GDR 2004 On dense granular flows. *Eur. Phys. J. E* **14** (4).

Miozzi, M., Jacob, B. & Olivieri, A. 2008 Performances of feature tracking in turbulent boundary layer investigation. *Exper. Fluids* **45** (4), 765–780.

Moreau, J.J. 1994 Some numerical methods in multibody dynamics: application to granular materials. *European J. of Mech. A/Solids* **13** (4-suppl), 93–114.

Moretti, L., Mangeney, A., Capdeville, Y., Stutzmann, E., Huggel, C., Schneider, D. & Bouchut, F. 2012 Numerical modeling of the mount steller landslide flow history and of the generated long period seismic waves. *Geophys. Res. Lett.* **39** (16).

Naaim, M., Faug, T. & Naaim-Bouvet, F. 2003 Dry granular flow modelling including erosion and deposition. *Surv. Geophys.* **24** (5), 569–585.

Narain, R., Golas, A. & Lin, M. C. 2010 Free-flowing granular materials with two-way solid coupling. In *ACM Trans. Graph.*, , vol. 29, p. 173. ACM.

Pouliquen, O. 1999 Scaling laws in granular flows down rough inclined planes. *Phys. Fluids* **11** (3), 542–548.

Pouliquen, O. & Forterre, Y. 2002 Friction law for dense granular flows: application to the motion of a mass down a rough inclined plane. *J. Fluid Mech.* **453**, 133–151.

Rousseau, G. & Ancey, C. 2020 Scanning PIV of turbulent flows over and through rough porous beds using refractive index matching. *Exper. Fluids* **61** (8), 1–24.

Russell, A.S., Johnson, C.G. .and Edwards, A.N., Viroulet, S., Rocha, F.M. & Gray, J.M.N.T. 2019 Retrogressive failure of a static granular layer on an inclined plane. *J. Fluid Mech.* **869**, 313–340.

Savage, S. B. 1979 Gravity flow of cohesionless granular materials in chutes and channels. *J. Fluid Mech.* **92** (1), 53–96.

Shi, Jianbo 1994 Good features to track. In *1994 Proceedings of IEEE conference on computer vision and pattern recognition*, pp. 593–600. IEEE.

Silbert, L.E., Ertaş, D., Grest, G.S., Halsey, T.C., Levine, D. & Plimpton, S.J. 2001 Granular flow down an inclined plane: Bagnold scaling and rheology. *Phys. Rev. E* **64** (5), 051302.

Staron, L. & Hinch, E.J. 2005 Study of the collapse of granular columns using two-dimensional discrete-grain simulation. *J. Fluid Mech.* **545**, 1–27.

Sulsky, D., Zhou, S.-J. & Schreyer, H. L. 1995 Application of a particle-in-cell method to solid mechanics. *Comput. Phys. communications* **87** (1-2), 236–252.

Taberlet, N., Richard, P., Valance, A., Losert, W., Pasini, J. M., Jenkins, J. T. & Delannay, R. 2003 Superstable granular heap in a thin channel. *Phys. Rev. Lett.* **91** (26), 264301.

Valette, R., Riber, S., Sardo, L., Castellani, R., Costes, F., Vriend, N. & Hachem, E. 2019 Sensitivity to the rheology and geometry of granular collapses by using the μ (I) rheology. *Computers & Fluids* **191**, 104260.

Zhang, R., Su, D., Lei, G. & Chen, X. 2021 Three-dimensional granular column collapse: Impact of column thickness. *Powder Technol.* **389**, 328–338.